S.T. Yau High School Science Award

Research Report

The Team

Name of team member: Qianxun Zhao
School: Phillips Academy Andover
City, Country: Andover, USA

Name of supervising teacher: TianFu Fu
Job Title: Research Scientist
School/Institution: Meta AI
City, Country: USA

Title of Research Report

Bistability and Negative Stiffness of Truncated-Conical Shell

Date

[08/18/2023]

Bistability and Negative Stiffness of Truncated-Conical Shell

Qianxun Zhao

August 19, 2023

Abstract

In this paper, a parametric simulation analysis method for truncated-conical shells was presented, it was developed using the Python language combined with the finite element method. Our discussion primarily delves into the deformation characteristics of these shells, as influenced by their materials, geometry, and boundary conditions. The deformation theory of the truncated-conical shell was established, elucidating the internal mechanisms behind its bistable state and negative stiffness deformation traits. Through an integrated script for batch modeling and data processing, the deformation characteristics of various truncated-conical shells were discerned. Leveraging the dimensional analysis method and extensive simulation results, the quantitative expressions for both the dimensionless bistable critical thickness and negative stiffness critical thickness of the truncated-conical shell were derived. Moreover, quantitative descriptions of the associated characteristic forces were provided. The analytical findings were validated with experimental results obtained from 3D-printed truncated-conical shells.

keyword: Truncated-conical shell, FEM, Bistable, Negative stiffness

Declaration of Academic Integrity

The participating team declares that the paper submitted is comprised of original research and results obtained under the guidance of the instructor. To the team's best knowledge, the paper does not contain research results, published or not, from a person who is not a team member, except for the content listed in the references and the acknowledgment. If there is any misinformation, we are willing to take all the related responsibilities.

Names of team members Qianxun Zhao

Signatures of team members Qianxun Zhao

Name of the instructor Tianfu Fu

Signature of the instructor Tianfu Fu

Date 08/15/2023

Commitments on Academic Honesty and Integrity

We hereby declare that we

1. are fully committed to the principle of honesty, integrity and fair play throughout the competition.
2. actually perform the research work ourselves and thus truly understand the content of the work.
3. observe the common standard of academic integrity adopted by most journals and degree theses.
4. have declared all the assistance and contribution we have received from any personnel, agency, institution, etc. for the research work.
5. undertake to avoid getting in touch with assessment panel members in a way that may lead to direct or indirect conflict of interest.
6. undertake to avoid any interaction with assessment panel members that would undermine the neutrality of the panel member and fairness of the assessment process.
7. observe the safety regulations of the laboratory(ies) where we conduct the experiment(s), if applicable.
8. observe all rules and regulations of the competition.
9. agree that the decision of YHSA is final in all matters related to the competition.

We understand and agree that failure to honour the above commitments may lead to disqualification from the competition and/or removal of reward, if applicable; that any unethical deeds, if found, will be disclosed to the school principal of team member(s) and relevant parties if deemed necessary; and that the decision of YHSA is final and no appeal will be accepted.

(Signatures of full team below)

Qianxun Zhuo

Name of team member:

Tianfu Fu

Name of supervising teacher:

Contents

1 Introduction

In the absence of external loads, most structures encountered in daily life exhibit only a single stable state. However, certain structures can be stably maintained in two or more equilibrium states, making them bistable or multistable. These multistable structures can transition between multiple stable states under appropriate stimuli or loads. For instance, the leaves of Venus flytraps possess two stable states: open and closed. They capture insects by toggling between these states[2]. Everyday items like hairpins, tape measures, and straws also exhibit multiple stable states, greatly facilitating human activities. Characterized by the ability to preserve multiple equilibrium states and swiftly transition between them while releasing energy, multistable structures hold significant potential in applications such as actuators, robots, energy harvesters, and sensors[1].

Figure 1(c) depicts how the energy of a bistable structure rises, subsequently diminishes, and then rises again during the loading process. The gradient of the energy-displacement curve reflects the force magnitude. Consequently, as the structure is loaded, the force first intensifies, then declines to a negative value before rising again. This means the gradient of the force-displacement curve assumes a negative value during the bistable structure's loading, with its relative minimum value being less than zero. Conversely, Figure 1(a) illustrates the force-displacement curve of most monostable structures, where the force progressively increases with displacement, indicating positive stiffness. If the force in a monostable structure first rises, then reduces, and rises again with displacement (as in Figure 1(b)), the structure manifests negative stiffness. Structures with negative stiffness are typically harnessed in designing energy absorption and vibration isolation devices. Common straws, for instance, can assume multiple geometric states, classifying them as multistable structures[5]. Upon close inspection, the deformable section of a straw consists of a series of truncated-conical shells. Each of these shells can exhibit two stable states, inverting either inward or outward. This lends straws their multistable nature. Previous research on truncated-conical shells has primarily focused on their deformation response under singular boundary constraints and within a limited size spectrum[5, 4, 7]. This paper embarks on a comprehensive exploration of truncated-conical shells under diverse boundary conditions across a broader size range, emphasizing their bistable and

Figure 1: Different States Of Structures

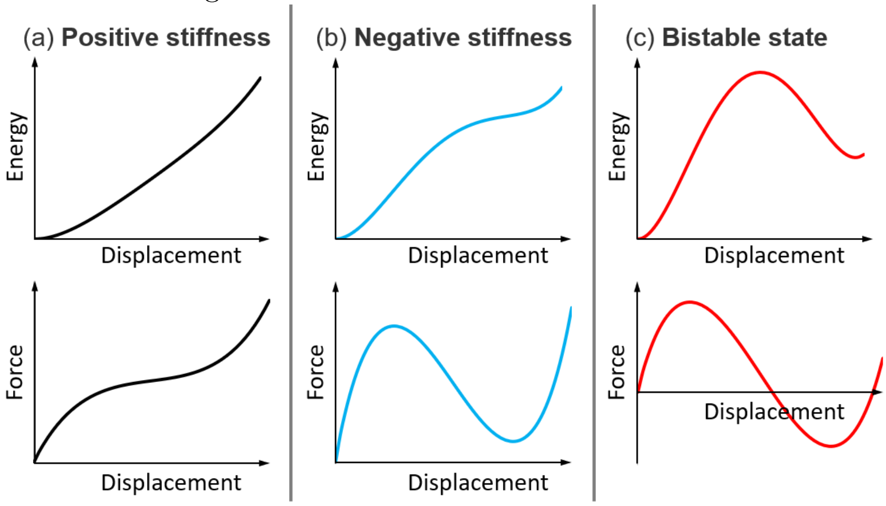

negative stiffness responses.

The subsequent sections are structured as follows: Section two introduces the deformation analysis process of the truncated-conical shell, detailing its bistability. Section three proposes a parametric modeling analysis calculation method rooted in the Python language, elaborating on how materials, geometry, and boundary constraints influence the deformation of the truncated-conical shell. Section four formulates the deformation theory of truncated-conical shells, dissecting the internal mechanisms underpinning structural bistability. In section five, leveraging data from batch calculations, we establish quantitative relationships for the bistable critical thickness, negative stiffness critical thickness, and characteristic force under varying constraints, employing dimensional analysis. Finally, section six presents experiments using 3D-printed structures.

2 Analysis Method

To elucidate structural deformations, both experiments and simulations based on the finite element method (FEM) are commonly employed. While experimental methods offer valuable insights, finite element simulations often yield richer data and are more convenient to manage. As such, this study leverages the finite element simulation to delve into the structure of truncated-conical shells. Experimental verification of the findings is provided in section 6.

2.1 Physical Model

The truncated-conical shell structure exhibits rotational symmetry, making it a kind of rotary structure, as depicted in Figure 2.

Figure 2: Geometric Schematic Diagram of Truncated-Conical Shell

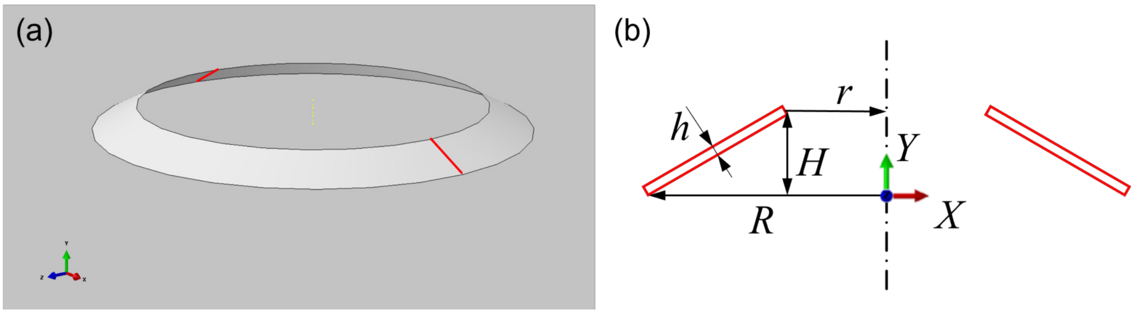

This structure is characterized by four geometric parameters: the larger circle radius R, the smaller circle radius r, the altitude difference H, and the shell thickness h.

In the subsequent subsection, the FEM will be employed to highlight the presence of two distinct, reversible stable states inherent to this structure.

2.2 Finite Element Modeling

For the structural deformation analysis, the Abaqus software, which utilizes FEM, is chosen. Initially, shell elements are used to construct a truncated-conical shell (as visualized in Figure 2 with dimensions ($R = 10mm, r = 8mm, H = 1mm, h = 0.2mm$). Subsequently, the structure is rotated 180° about the $x-axis$, ensuring that the loading direction aligns with the positive Y-axis direction.

Figure 3: Reversed Structure

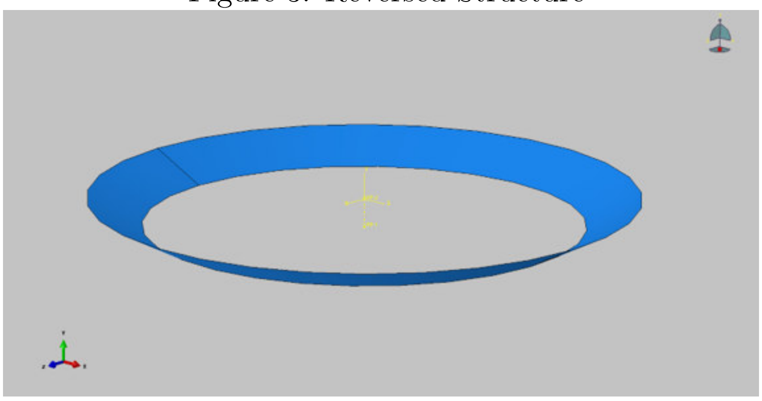

Following this, material properties are introduced with an elastic modulus $E = 1MPa$ and a Poisson's ratio $\nu = 0.3$.

Two reference points are then formulated, which establish a coupling relationship with the larger and smaller circles, respectively. This coupling is restricted to the Y-direction displacement, as illustrated in Figure 4.

Figure 4: Coupling Relationship

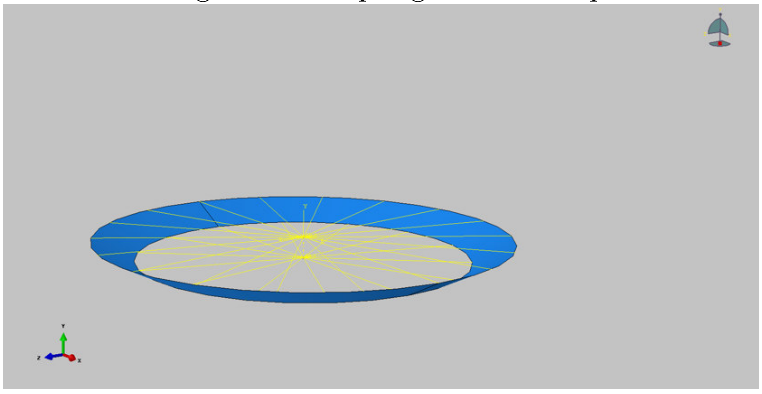

The analysis encompasses two steps. The primary step involves inverting the structure, during which displacement boundary conditions are applied to both circles via the reference points. Their Y-direction displacements are set to 0 and $2H$, respectively. In the subsequent step, the external load is relinquished, allowing observation of the structural transformation.

The structure is then meshed for computational processing with a mesh density of $0.2mm$. The resultant meshed structure is portrayed in Figure 5.

Figure 5: The Meshed Structure

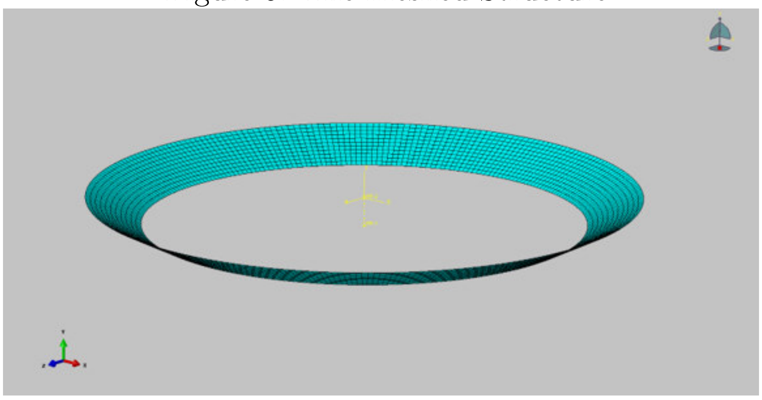

To conclude the process, a job is instantiated, and the computation results are subsequently collated.

2.3 Analysis Results

Following the aforementioned calculations, the deformational shapes of the truncated-conical shell were captured, as illustrated in Figure 6:

Figure 6: The Loading Process of The Truncated-Conical Shell

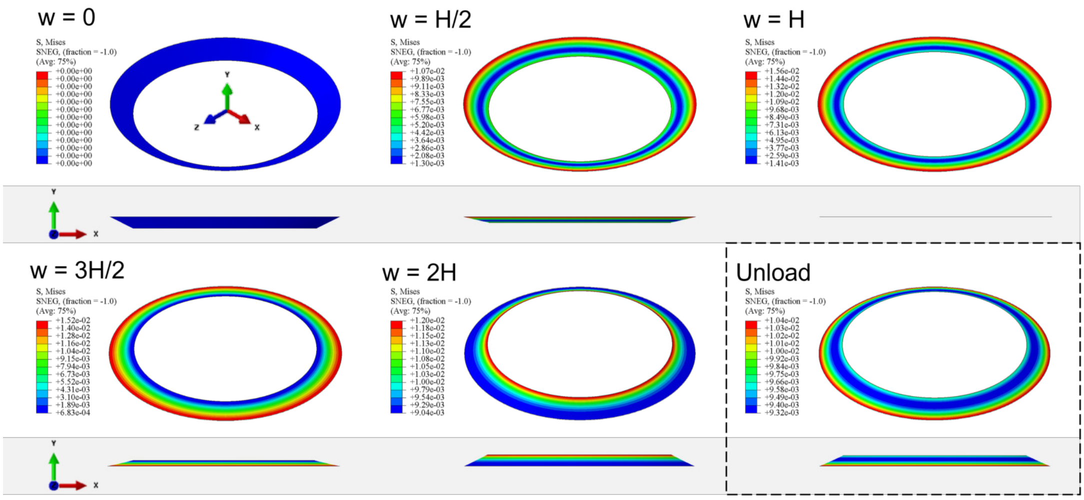

It is found that as the loading progressed, the structure flipped inside out, and the structure remained flipped after unloading. This shows that the structure can stay flipped stably, which shows that the structure has bistable characteristics.

2.4 Data Extraction and Analysis

Based on the computational findings, the relationship curves between force F, deformation energy U, and loading displacement w were plotted, as seen in Figure 7: As the loading displacement increases in the first stage, both the energy and force

Figure 7: The Force-displacement curve and Deformation Energy-displacement curve

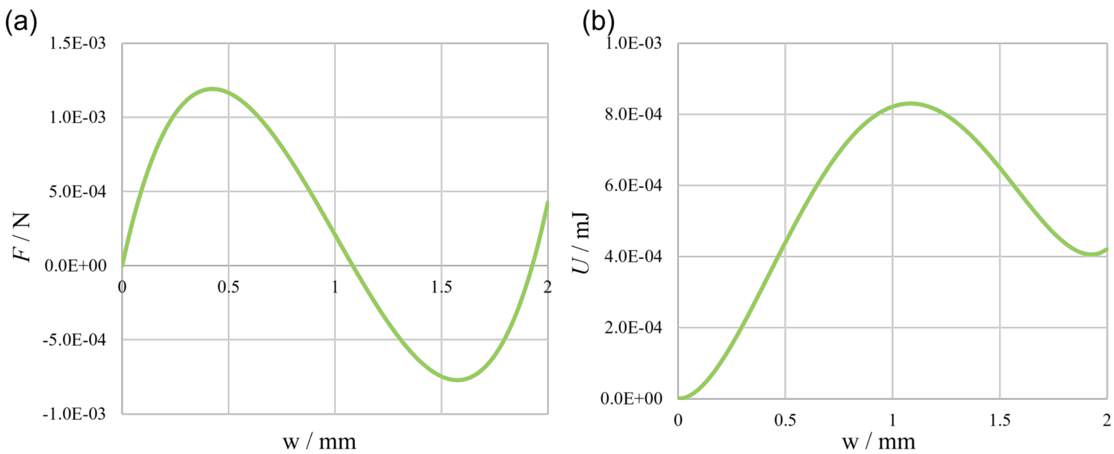

values also increase. In the second stage, the value of the force increases to a relative maximum value and gradually starts to decrease to zero. As the force value drops to zero, the deformation energy of the structure reaches its peak. Then, in the third stage, the value of the force is negative, and the magnitude of the force starts off by increasing and then decreases to zero. The deformation energy of the structure can be gradually reduced to a relative minimum value. Lastly, in the fourth stage, the value of the force is positive and the deformation energy continues to increase.

2.5 Effects Of Mesh Density

Mesh density plays a pivotal role in influencing FEM computational accuracy. Thus, it's imperative to ensure the mesh granularity is optimal. As depicted in Figure 8, various mesh sizes - $0.2, 0.15, 0.10$, and 0.05 - were applied to the structure, followed by subsequent calculations.

Figure 8: The Structure with Different Mesh Sizes

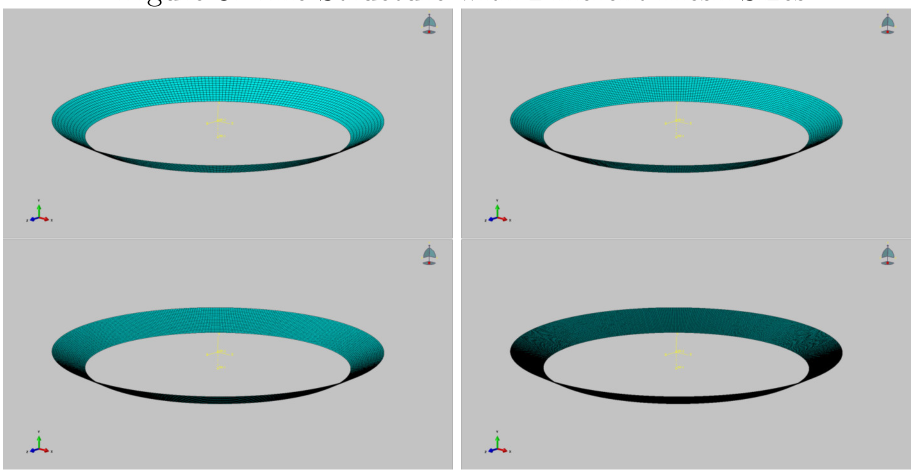

Figure 9 reveals that variations in mesh density impart negligible deviations in the results. To strike a balance between accuracy and computational efficiency, a mesh density of $0.2mm$ is chosen.

3 Influence Of Different Materials, Geometry, and Boundary Conditions

The factors that may affect the deformation characteristics are geometric parameters, material parameters, and boundary conditions. This section first creates a script

Figure 9: Force-Displacement Curves with Different Mesh Sizes

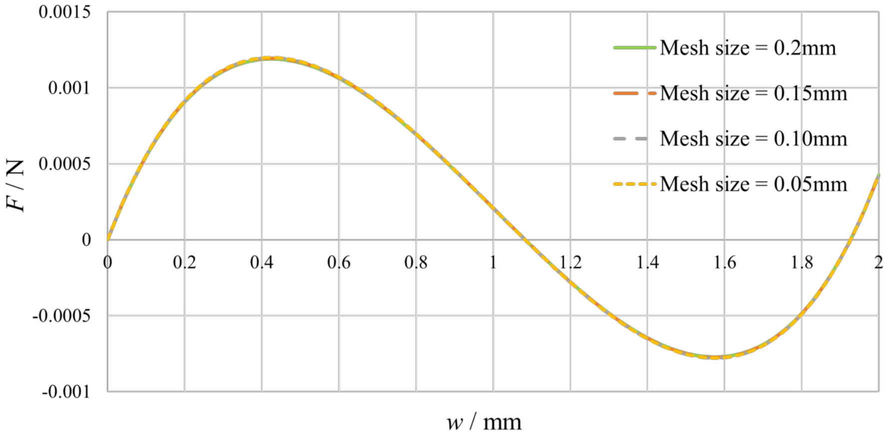

file based on Python language to realize parametric modeling so that it's possible to explore the impact of the parameters. The advantage of using scripts is that it will make our modeling more convenient and realize batch automatic calculation.

3.1 Parametric Modeling Script

In order to realize the parametric modeling in the above process, a script suitable for Abaqus software is written based on Python language[6]. After the parameters are given, the script is run through the Abaqus software to realize the automatic modeling, calculation, and data extraction of the above analysis. Based on the loop statement, batch calculation of various parameters can also be realized.

3.2 Influence of Material Parameters on Structural Deformation

Two different material parameters are mainly considered: elastic modulus E and Poisson's ratio ν. Based on the script file, the deformation responses of multiple structures with different elastic modulus values and Poisson's ratio values are calculated respectively.

Based on the settings in section 2, the script in the previous section is used to calculate the deformation response of the structure with the elastic modulus of $1MPa, 2MPa, 3MPa, 4MPa$, and $5MPa$. Figure 10 illustrates the structural deformation curves of force and energy with respect to displacement for different elastic modulus values.

Figure 10: Force-Displacement Curves with Different Elastic Moduli

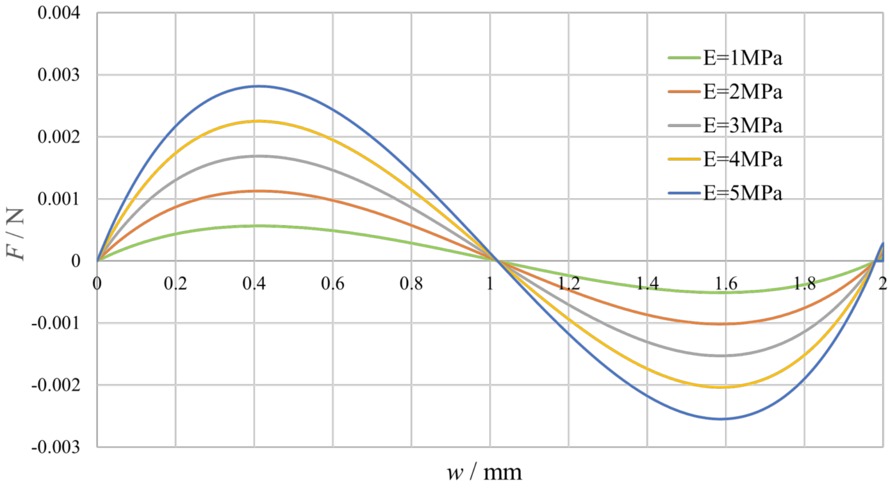

It can be clearly seen from Figure 10 and Figure 11 that the shapes of the force and energy curves do not change with the change in elastic modulus. With a higher modulus of elasticity, more force is required during loading, and at the same time the structure stores more energy.

Figure 11: Deformation Energy-Displacement Curves with Different Elastic Modulus

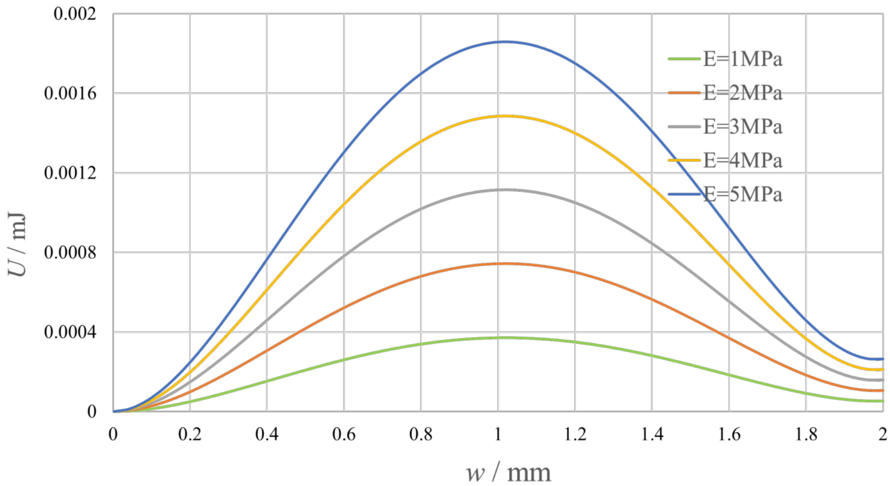

After combining the data analysis, the curves of F/E and U/E with w are shown in Figure 12. It is found that when the elastic modulus of the structure changes k times, the external force and deformation energy required in the deformation process becomes k times the original. In layman's terms, U and F become larger as many times as E changes. During the drawing, F/E is used. This is equivalent to removing the multiples of the influencing factors, so the curves in Figure 12 are coincident. The conclusion is that no matter how E changes, the ratio of F to E remains the same.

Figure 12: (a)Relationship Curves Between F/E and w; (b)Relationship Curves Between U/E and w

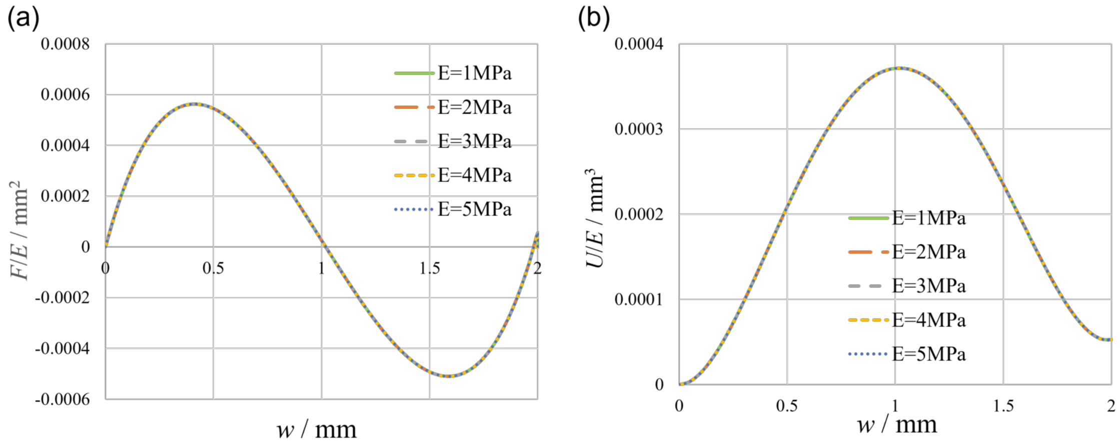

The size and elastic modulus of the structure remain unchanged, and the deformation response of the structure is shown in Figure 13 when Poisson's ratio are $0.2, 0.25, 0.3, 0.35$, and 0.4.

Figure 13: Force-Displacement Curves with Different Poisson's ratios

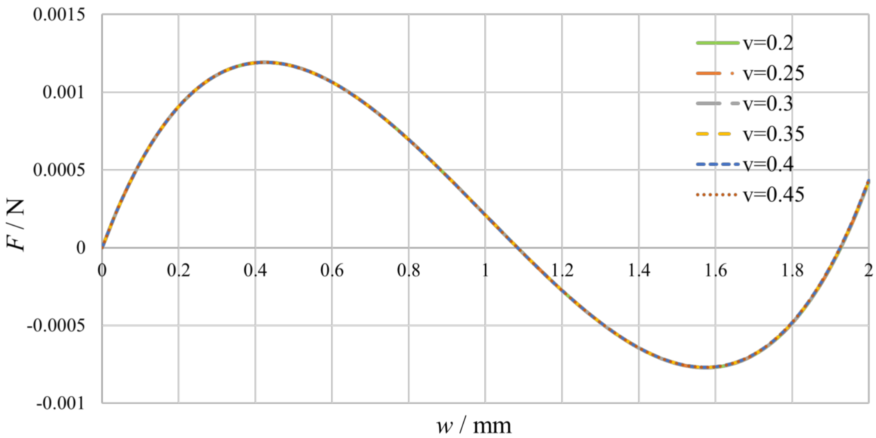

The curves in Figure 13 almost overlap. Therefore, it is found that no matter what the value of Poisson's ratio is, it will not affect the deformation force of the structure.

3.3 Influence of Geometric Parameters on Structural Properties

The shape of a truncated-conical shell is determined by R (great circle radius), r (small circle radius), H (altitude difference), and h (shell thickness). This section discusses the deformation response of truncated-conical shells with different geometric parameters. The deformation characteristics of the geometrically similar truncated-conical shells are examined first. It is found that they have geometrically similar characteristics, that is, the four geometric parameters are proportional. On the basis of the size of the geometric model in section 2, let the overall enlargement be 2 and 3 times. The 4 parameters are also doubled and tripled. The calculation results are shown in Figure 14.

Figure 14: Deformation Characteristics with Different Magnification Times

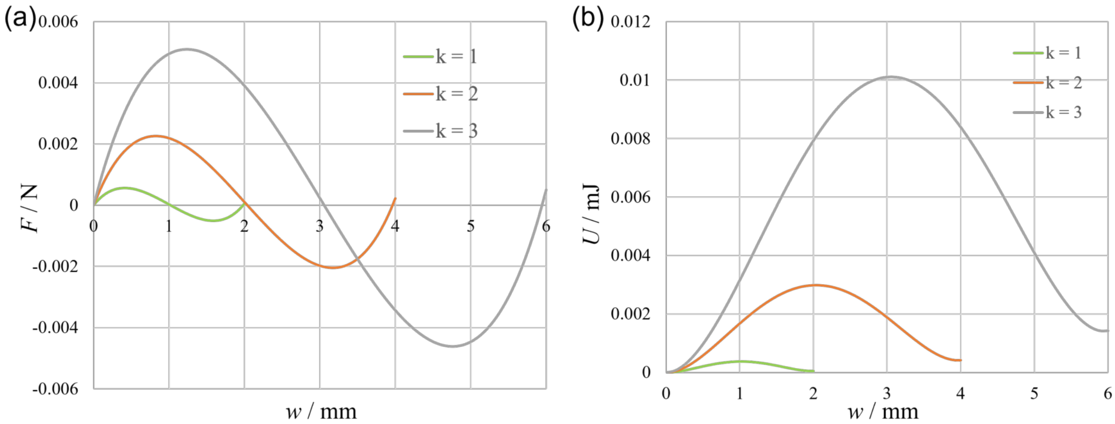

As shown in Figure 14, the altitude difference H of these three similar structures is different, so the displacement during loading is also different. Therefore, a dimensionless loading displacement $\bar{w} = w/H$ is defined in the figure, the purpose is to unify the loading displacement of structures with different geometric sizes(see Figure 15).

Figure 15: (a)Relationship Curves Between F and $\bar{w}$; (b)Relationship Curves Between U and $\bar{w}$

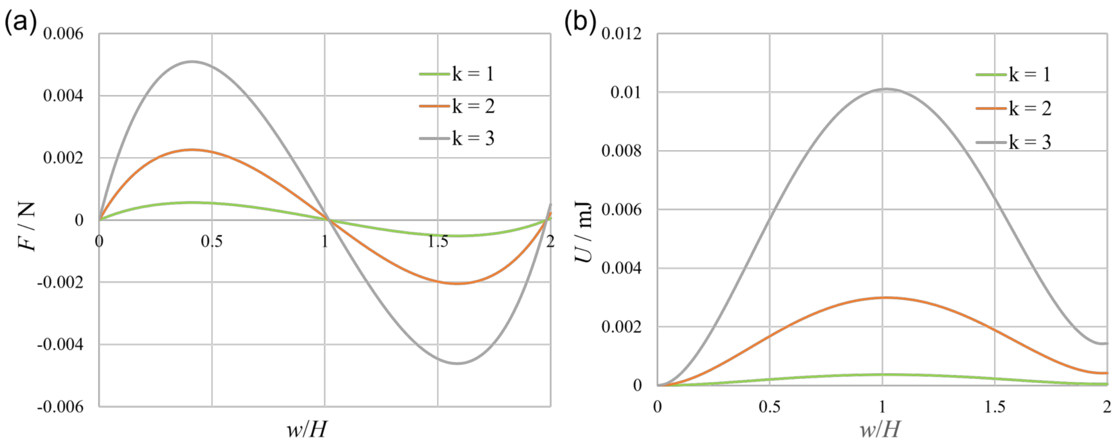

Through the analysis of specific data, it is found that when the overall size of the geometric structure is enlarged by k times, the force and energy in the loading process are respectively enlarged by k^2 times and k^3 times(see Figure 16). It can be concluded that different truncated-conical shells with similar geometry have similar deformation characteristics. This means that the deformation analysis for a truncated-conical shell of one size is also applicable to all other structures with similar geometry.

Figure 16: (a)Relationship Curves Between F/k^2 and $\bar{w}$; (b)Relationship Curves Between U/k^3 and $\bar{w}$

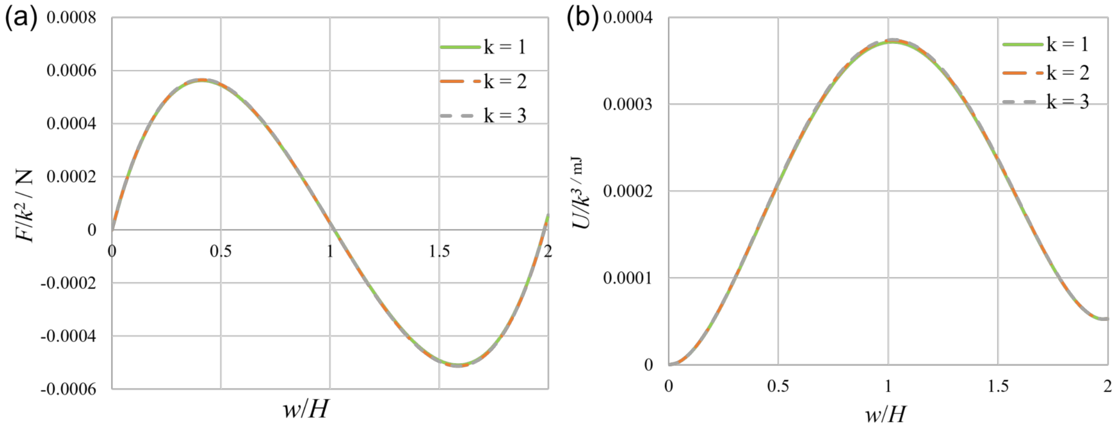

Figure 17: Force-Displacement Curves with Different Height Differences

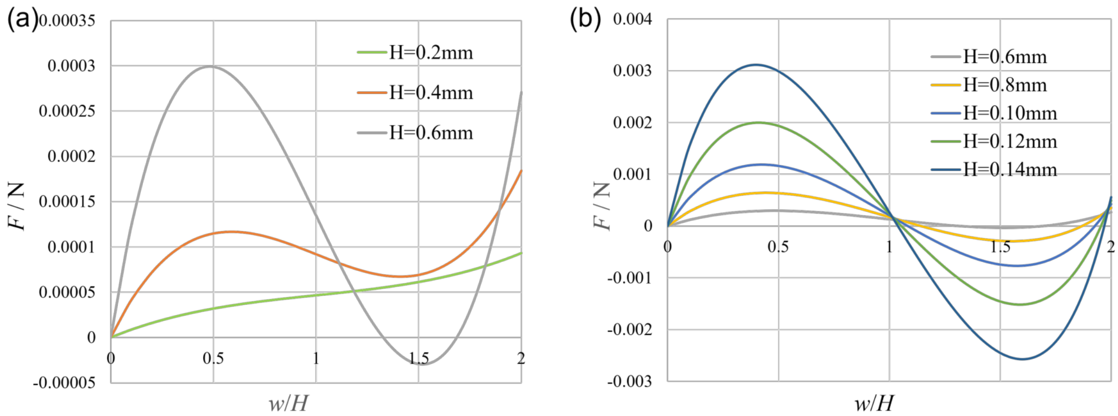

Firstly, the influence of height h on structural deformation characteristics is analyzed. Keeping R, r, and h unchanged, the altitude difference H has the value from $0.2mm$ to $1.4mm$, and the interval of each height is $0.2mm$.

As shown in Figure 17, when $H = 0.2mm$, the force increases with the increase of the loading displacement until the structure is completely overturned. This shows that the structure at this time has positive stiffness and no bistable characteristics. The structure has negative stiffness but no bistability as $H = 0.4mm$. When H is greater than or equal to 0.5mm, the structure is bistable, and the larger h, the greater the force required for steady-state switching.

As shown in Figure 18, keep R, H, and h unchanged. The force-displacement curves have the same shape, both have bistability properties. With the increase of r, the bistable characteristics become more obvious, which means that a larger force is needed to make it flip to the second stable state. With the increase of r, the force of the loading process increases, and the increase rate becomes faster.

Figure 18: Force-Displacement Curves with Different Small Circle Radii

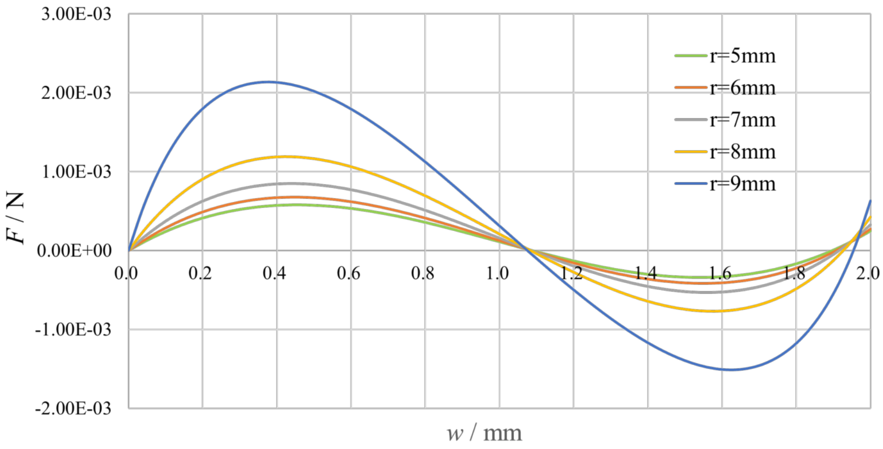

Figure 19: Force-Displacement Curves with Different Thicknesses

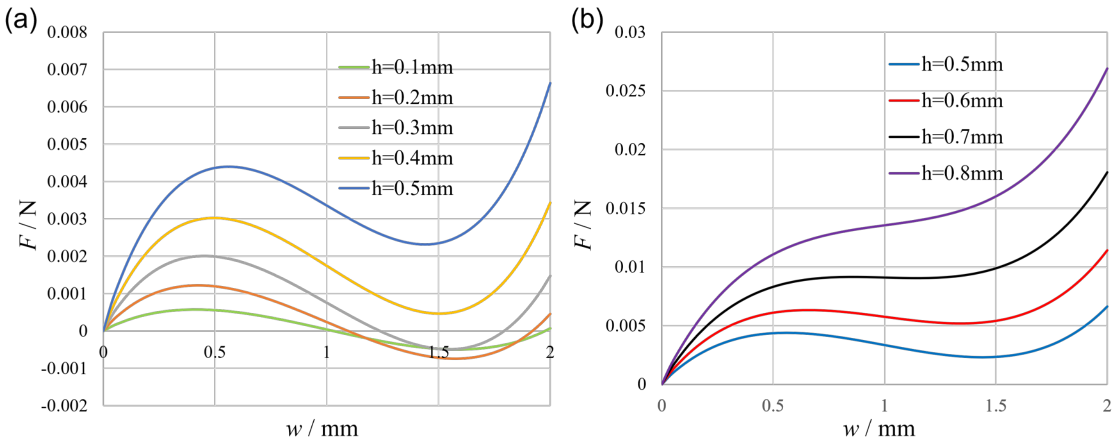

Then the influence of shell thickness h on the deformation characteristics of the structure is analyzed. As shown in Figure 19, when $h = 0.1mm, 0.2mm, 0.3mm$, the structure is bistable, but the structure with $h = 0.4mm$ or $h = 0.5mm$ is monostable. As h increases, the structure changes from bistability to having negative stiffness to having positive stiffness.

In summary, it can be found that if the geometrically similar truncated-conical shell structures are similar, the mechanical properties are also similar. As the ratio of height to the radius of the great circle increases under the chosen geometric size, the structure will change gradually from positive stiffness to negative stiffness, eventually reaching a bistable state. All radius of small circle has bistability, which becomes more pronounced as the ratio of small circle radius to great circle increases. As the ratio of shell thickness to great circle increases, the structure changes from bistability to negative stiffness and then to positive stiffness again. The truncated-conical shell with a large altitude difference, large radius of a small circle, and small thickness is bistable. The truncated-conical shell is bistable when it has a large altitude difference, a large small circle radius, and a thin shell.

3.4 Effect of Boundary Conditions

In this section, the influence of the small circle and great circle displacement boundary condition constraints on the truncated-conical shell is focused. As shown in Figure

Figure 20: Different Boundary Conditions

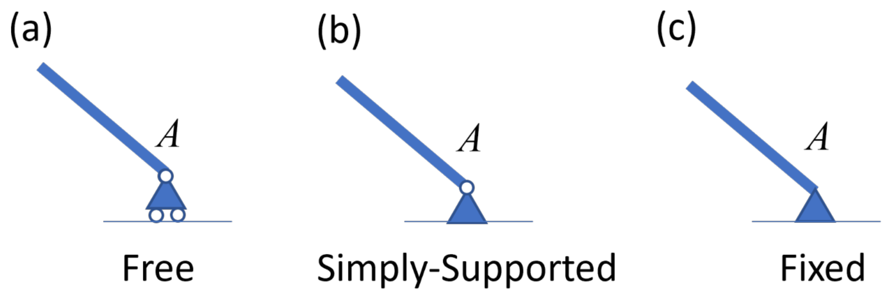

20(a), the structure is in free boundary condition at point A, that is, it can move and rotate freely. As depicted in Figure 20(b), the structure is under simply supported boundary conditions at point A, and its left and right movement is restricted, but it can rotate freely. As shown in Figure 20(c), the structure is under fixed boundary conditions at point A, which means it can neither move nor fan be turned. Nine boundary conditions are possible for truncated-conical shells. Based on the geometric dimensions in section 2, the different boundary conditions are applied to the small circle and the great circle, and the calculation is submitted. The calculation result is shown in Figure 21.

The force-displacement curves of truncated-conical shells are quite different for different constraints, as illustrated in Figure 21. Therefore, when the small circle and

Figure 21: Force-Displacement Curves with Different Boundary Conditions

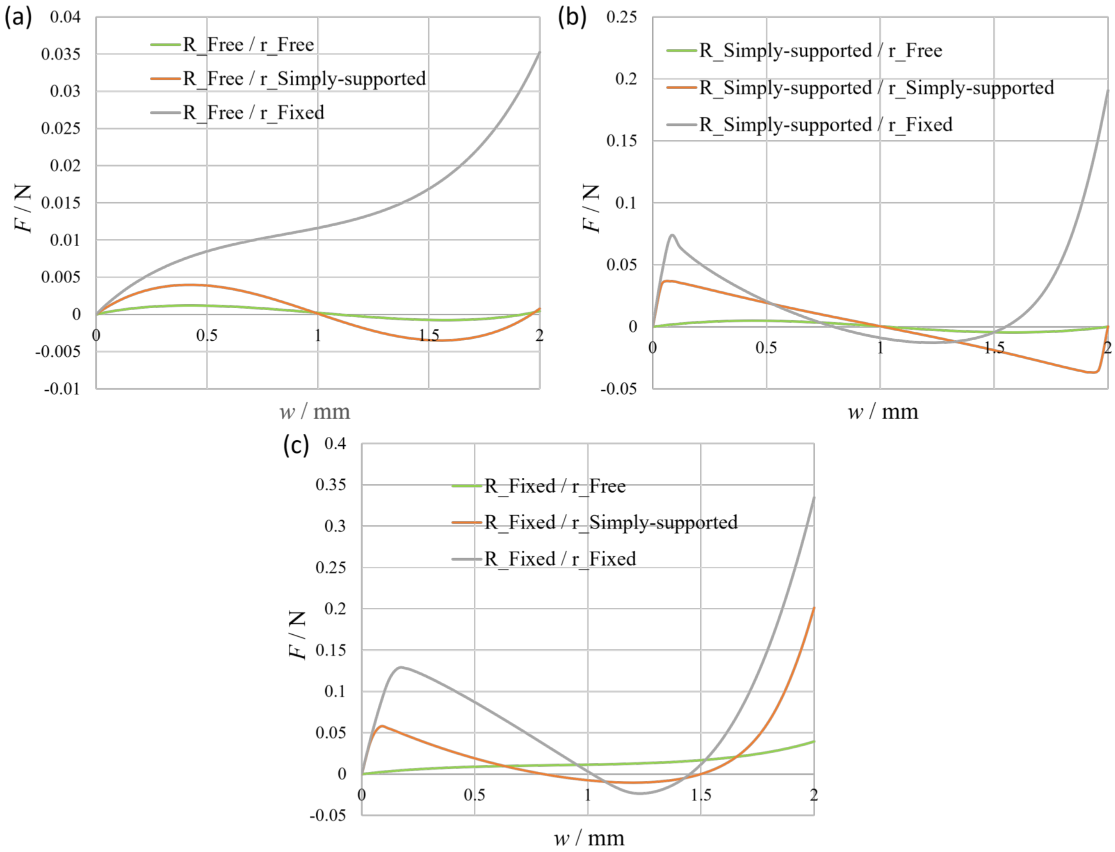

the great circle of the truncated-conical shells are under different boundary conditions, the mechanical properties of the structure are also different.

4 Bistable Mechanism Analysis

4.1 Deformation Theory with Double Free Boundary Conditions

As shown on the left side of Figure 22, the truncated-conical shell with $R = 10mm, r = 9mm, H = 1mm, h = 0.2mm$.

During the loading process, the cross-sectional shape of the truncated-conical shell is shown on the right side of Figure 22. It is found that the radius and perimeter of the small circle boundary decrease first and then increase during the loading process. On the other hand, the radius and perimeter of the great circle boundary display an initial increase followed by a decrease. This means that during loading, a hoop compressive deformation is found near the small circle boundary, while a hoop tensile deformation

Figure 22: Shape Change of Truncated-Conical Shell

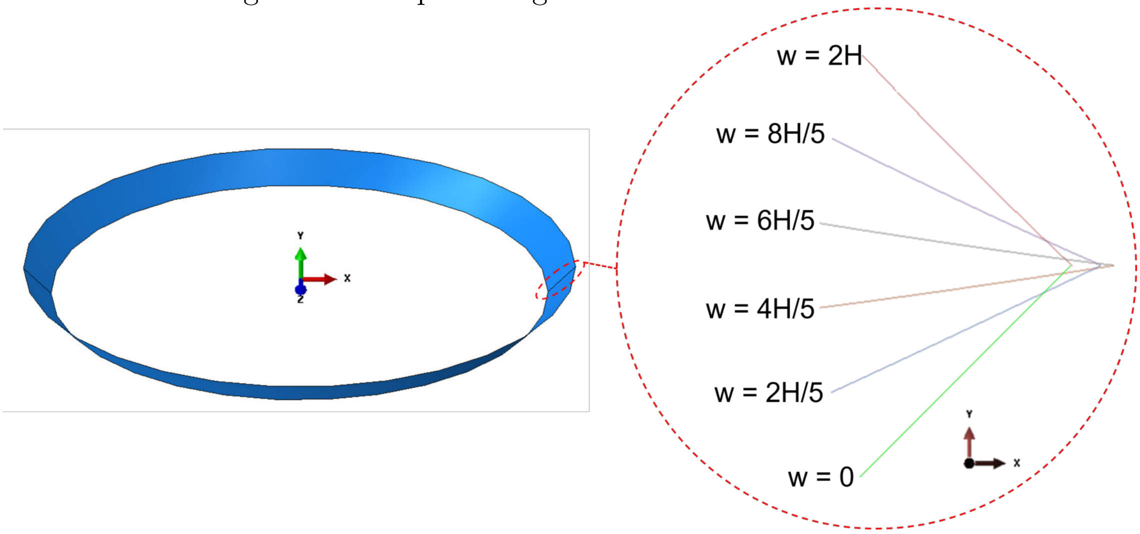

occurs near the large circle boundary. And during the loading process, the section of the truncated-conical shell is basically kept straight and the length is basically unchanged, that is, there is almost no bending deformation and tension-compression deformation in the radial direction. And the points on the inner surface experience an increase in perimeter, while the points on the outer surface experience a decrease in perimeter, resulting in circumferential bending deformation.

Figure 23: Schematic Diagram of Deformation

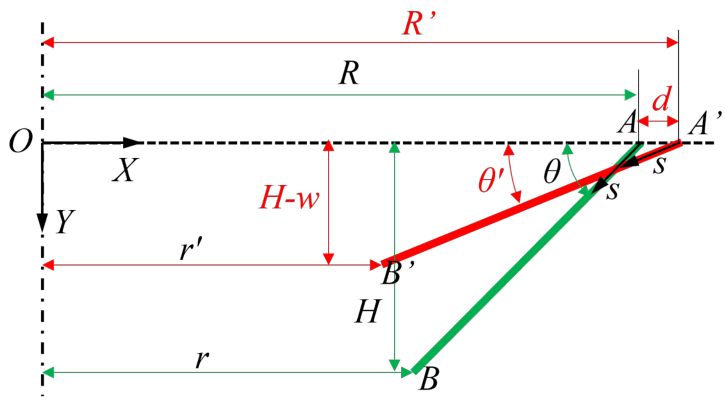

Figure 23 is a schematic diagram of the deformation of the centerline of the section of the truncated-conical shell before and after structural deformation. It is assumed that the section of the truncated-conical shell is always a straight line and the length is constant during the deformation process. The initial length L of the centerline is:

$$L = \sqrt{(R - r)^2 + H^2} \tag{1}$$

The inclination angle of the center line of the undeformed section, the circumferential curvature, and the coordinates of different positions are:

$$\sin\theta = \frac{H}{L} \tag{2}$$

$$K_\phi = \frac{\sin\theta}{X} \tag{3}$$

$$X = R - s * \cos\theta \tag{4}$$

$$Y = s * \sin\theta \tag{5}$$

When the displacement is w, the radius increase of the great circle boundary of the structure is defined as d. Then the inclination angle of the center line of the deformed structure section, the circumferential curvature, and the coordinates of different positions can be expressed as[5]:

$$\sin\theta' = \frac{H - w}{L} \tag{6}$$

$$K'_\phi = \frac{\sin\theta'}{x} \tag{7}$$

$$x = R + d - s * \cos\theta' \tag{8}$$

$$y = s * \sin\theta' \tag{9}$$

The strain and curvature changes in the circumferential direction during the structural deformation process are[3]:

$$\varepsilon_\phi = \frac{x - X}{X} = \frac{d_0 + s * (\cos\theta_0 - \cos\theta)}{R - s * \cos\theta_0} \tag{10}$$

$$\Delta K_\phi = \frac{\sin\theta}{R + d_0 - s * \cos\theta} - \frac{\sin\theta_0}{R - s * \cos\theta_0} \tag{11}$$

Then the in-plane tension-compression strain energy and out-of-plane bending strain energy per unit area of the structure is:

$$u_{in} = \frac{1}{2} E h \varepsilon_\phi^2 \tag{12}$$

$$u_{out} = \frac{1}{2}\frac{Eh^3}{12(1 - v^2)}\Delta K_\phi^2 \tag{13}$$

The total in-plane tensile and compressive strain energy and out-of-plane bending strain energy of the structure obtained by integration are:

$$U_{in} = \int_0^{2\pi} \int_0^{L} u_{in}(R - s * \cos\theta) ds d\phi \tag{14}$$

$$U_{out} = \int_0^{2\pi} \int_0^{L} u_{out}(R - s * \cos\theta) ds d\phi \tag{15}$$

The total deformation energy of the structure is $U = U_{in} + U_{out}$, according to the principle of minimum potential energy ($\mathrm{d}U/\mathrm{d}d = 0$), the increase in radius d of the great circle boundary under different displacements can be obtained. Thus, the total deformation energy, in-plane deformation energy, and out-of-plane deformation energy of the structure under different displacements can be obtained.

Figure 24: Theoretical Results

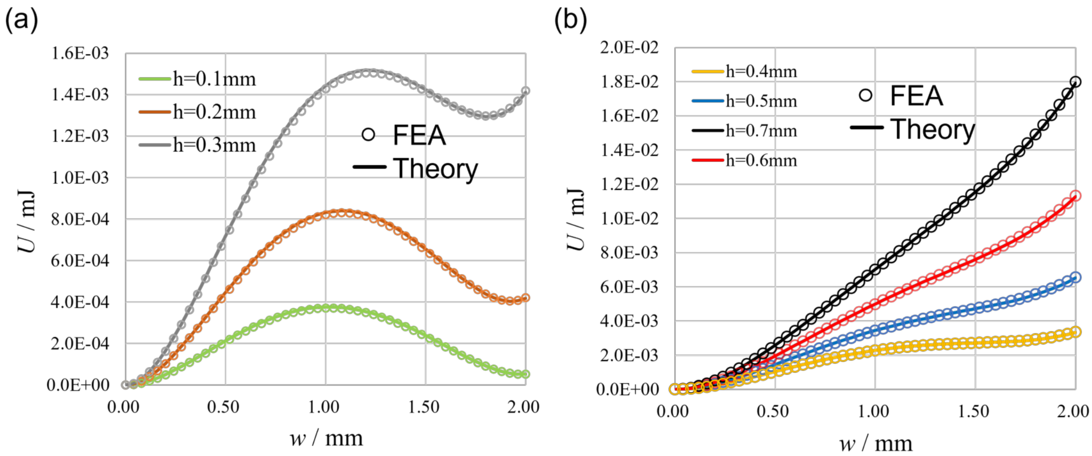

It can be seen from Figure 24 that the theoretical results of truncated conical shells with different thicknesses($R = 10mm, r = 8mm, h = 1mm$) are consistent with the finite element results.

4.2 Bistable Deformation Mechanism

As shown in Figure 25, the total energy U, the in-plane tensile and compressive deformation energy U_{in}, and the out-of-plane bending deformation energy U_{out} of the truncated-conical shell with $R = 10mm, r = 8mm, H = 1mm$, and $h = 0.2mm$ vary with the loading displacement. The figure illustrates a gradual increase in the in-plane deformation energy U_{in}, the out-of-plane deformation energy U_{out}, and the total energy

Figure 25: In-Plane and Out-of-Plane Deformation Energy

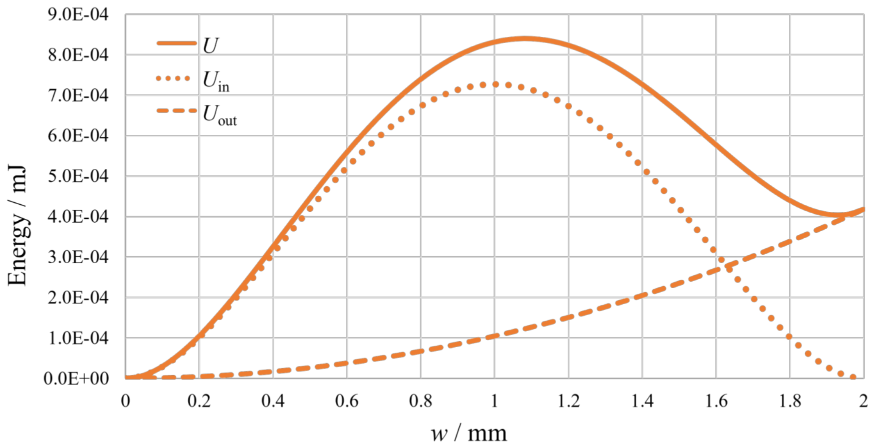

U as the thickness increases. For this structure, the in-plane deformation energy is much larger than the out-of-plane deformation energy, so the total energy and the in-plane deformation energy have the same deformation trend (increase first and then decrease). Therefore, the in-plane deformation energy dominates the total energy, and the structure has bistability.

Figure 26: (a) Energy Change With Different h; (b) U_{out}/U with Different h

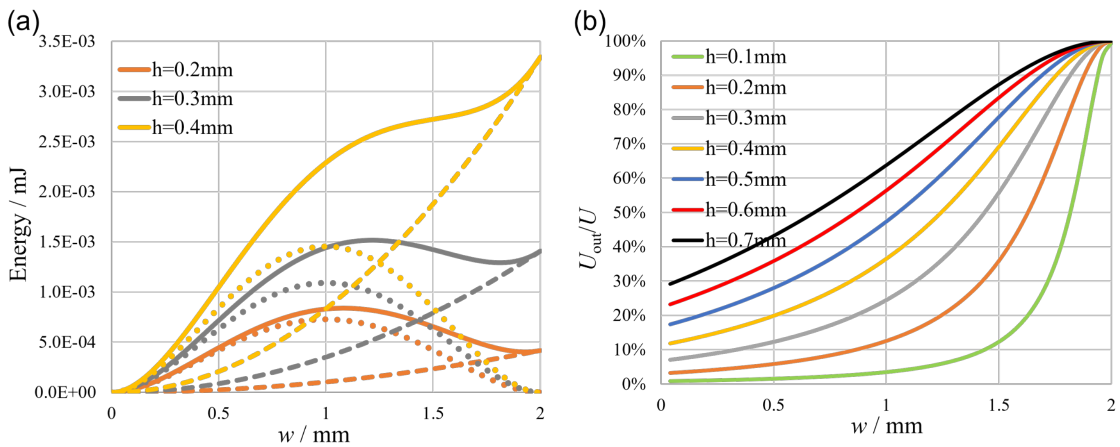

Figure 26(a) shows the energy change curves during the loading process of truncated-conical shells with different thicknesses ($R = 10mm, r = 8mm, H = 1mm$). As the thickness increases, U_{in}, U_{out}, and U increase gradually. Based on the previous theory, U_{in} is proportional to h, and U_{out} is proportional to h^3, so U_{out} increases faster with h. Figure 26(b) shows the ratio of out-of-plane deformation energy to total energy U_{out}/U for truncated-conical shells with different thicknesses. As the thickness increases, U_{out}/U increases, so the energy curve changes from a trend of first increasing and then decreasing to a gradually increasing trend, and the structure gradually changes from a bistable state is monostable.

Figure 27: U_{out}/U with Different r and H

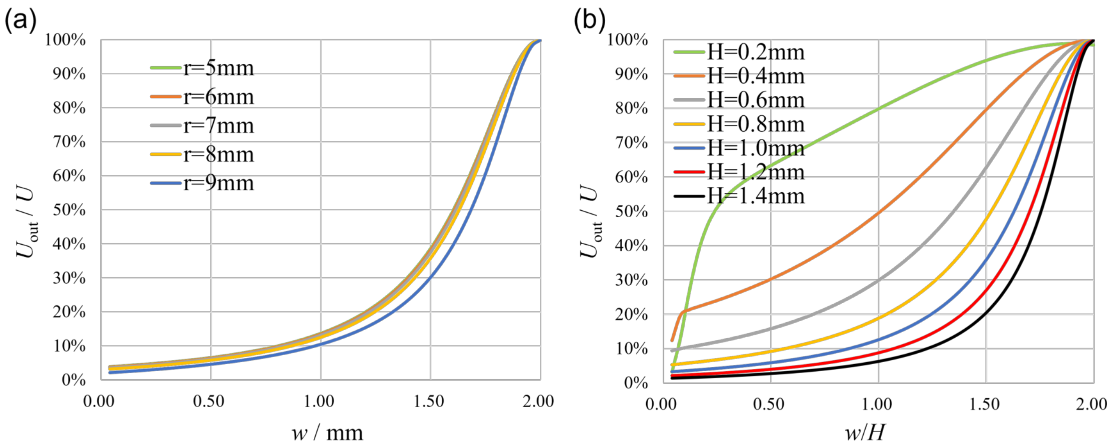

Figure 27(a) shows that the deformation process of truncated-conical shells with different radii is dominated by in-plane deformation energy, so the structures all have bistable states. Figure 27(b) shows that with the increase of height difference H, the proportion of out-of-plane deformation energy gradually increases, and the structure gradually changes from monostable to bistable.

4.3 Limitations of Deformation Theory

Figure 28: Comparison of Theoretical Results with FEA

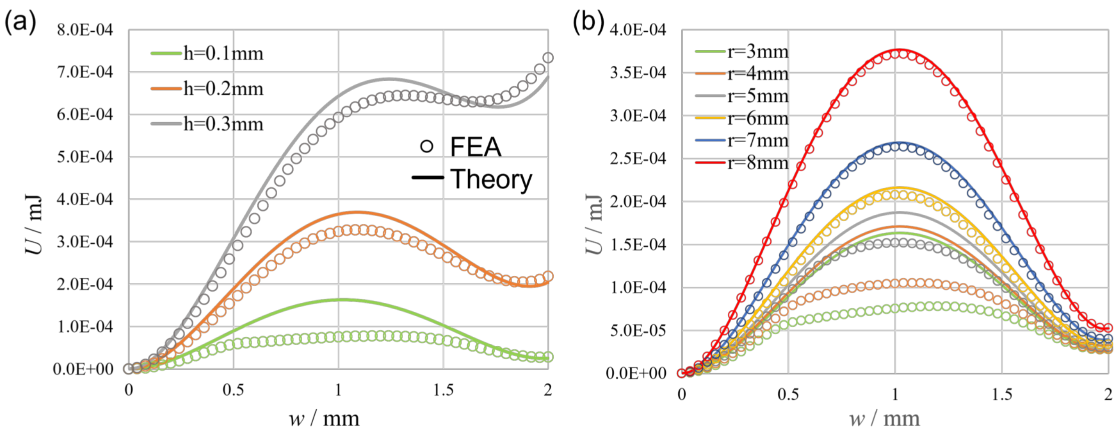

As shown in Figure 28(a), when $r = 3mm, h = 0.1mm(R = 10mm, H = 1mm)$, the error between theoretical and finite element results is obvious. As the thickness increases, the error decreases gradually. From Figure 28(b), it can be seen that for the truncated-conical shell with $R = 10mm, H = 1mm$, and $h = 0.1mm$, The above theory has a large error when r is small, and the error reduces as r increases. Therefore, the above theory cannot predict the deformation response of truncated-conical shell structures of all shapes under double-free boundary conditions.

Figure 29 is the morphology of the truncated-conical shell of $R = 10mm, r = 3mm, H = 1mm, h = 0.1mm$ when $w = h$. It can be seen that the section of the truncated-conical shell structure cannot keep a straight line during the deformation process. Therefore, the above theory cannot accurately predict the deformation response of the truncated-conical shell when both r and h are small.

Figure 29: Morphology of truncated-conical shell

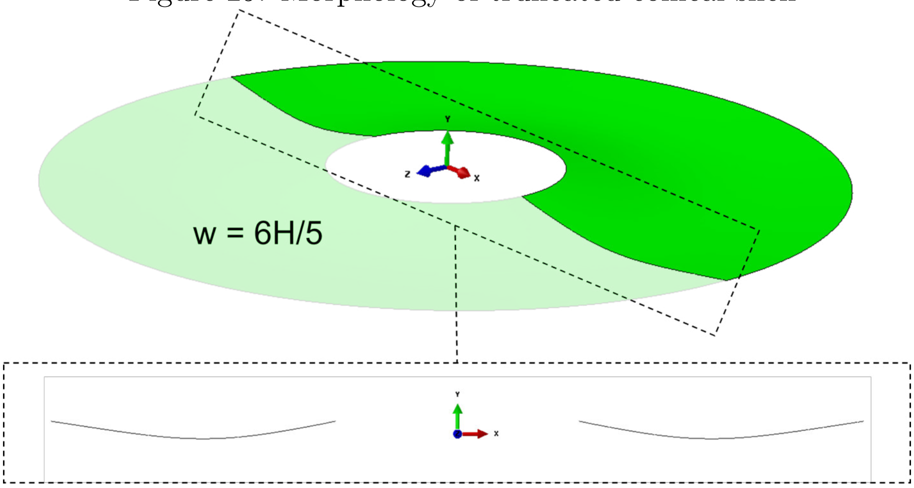

Figure 30: Deformation Process Under Double-Free Boundary Condition

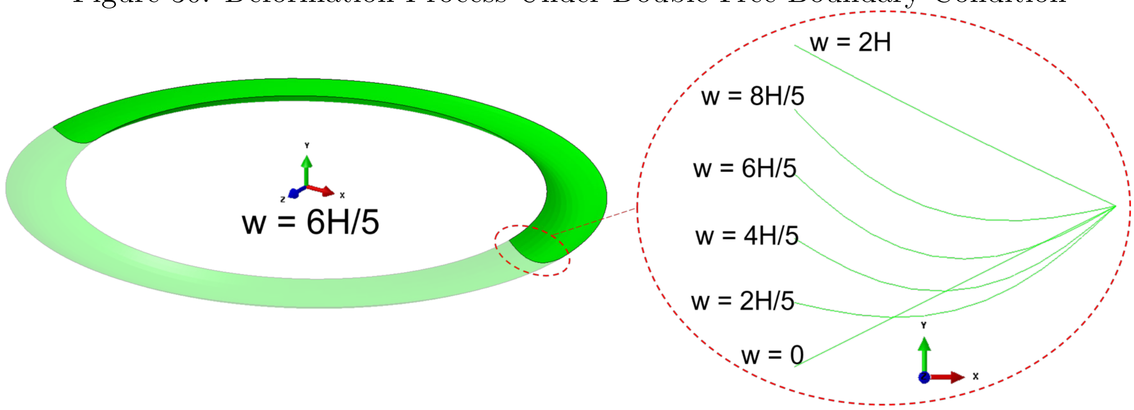

In addition, the boundaries and radii of the large and small circles of the truncated-conical shell cannot be changed in the case of double simple support. Figure 30 shows the shape of the truncated-conical shell structure ($R = 10mm, r = 8mm, H = 1mm, h = 0.2mm$) with $w = 6H/5$, and changes in the cross-section of the structure. It can be seen that due to the limitation of simply supported boundary, the cross-section of the deformed structure can not be kept straight.

Figure 31: Deformation Process Under Double-Supported Boundary Condition

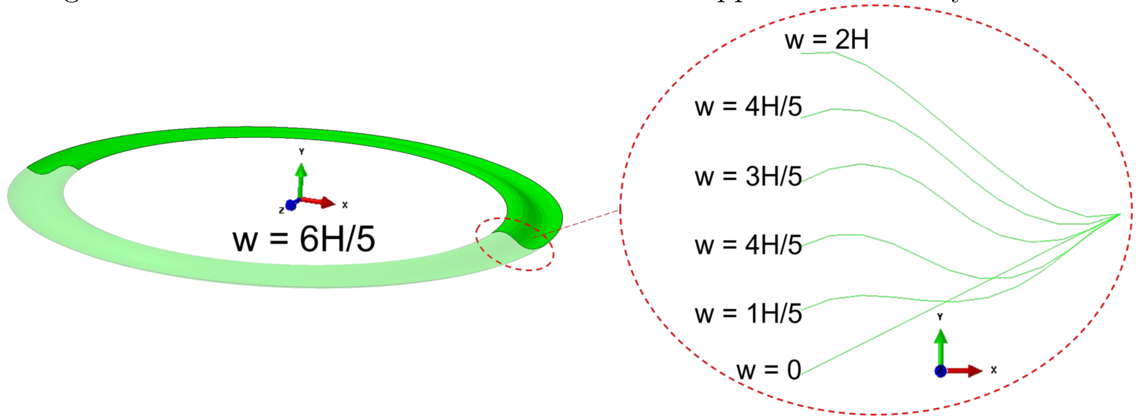

Figure 31 shows the deformation process of the cross-section of the truncated-conical shell under the double-supported condition. It can be found that due to the limitation of double-fixed boundary conditions, the radius of the structure boundary cannot be changed and cannot be rotated, so the structure section cannot keep a straight line.

It is very difficult to consider the radial bending of structures in theory, so the above theory can only be used to predict the deformation of most truncated-conical shells with the double-free boundary condition.

5 Quantitative Description of Structural Deformation of Truncated-Conical Shells

5.1 Dimensional Analysis

The research of section 3 shows that the deformation characteristics of the structure under certain boundary conditions are related to the geometric dimensions (R, r, H, h), material parameters (E), and characteristic forces (F_{char}). Their dimensions are:

$$\begin{aligned}
&[R] = L \\
&[r] = L \\
&[H] = L \\
&[h] = L \\
&[F_{char}] = MLT^{-2} \\
&[E] = ML^{-1}T^{-2}
\end{aligned} \tag{16}$$

For the above 6 physical quantities, there are 2 basic quantities: L and MT^2. It can be determined by the π theorem that the deformation characteristics of this structure can be described by four dimensionless parameters[8]. 4 dimensionless parameters are defined as follows:

$$\begin{aligned}
&\bar{F}_{char} = \frac{F_{char}}{ER^2} \\
&\bar{r} = r/R \\
&\bar{H} = H/R \\
&\bar{h} = h/R
\end{aligned} \tag{17}$$

They have a functional relationship:

$$\pi(\bar{F}_{char}, \bar{r}, \bar{H}, \bar{h}) = 0 \iff \bar{F}_{char} = F_{char}/ER^2 = g(\bar{r}, \bar{H}, \bar{h}) \tag{18}$$

It is found that the deformation characteristic force of the structure is determined by dimensionless height, thickness, and radius. Dimensionless geometric parameters do not change with modulus, so the dimensionless characteristic force remains unchanged. When the structure is scaled as a whole, the dimensionless radius, height, and thickness do not change, so the dimensionless characteristic force does not change either.

5.2 Double Free Boundary Conditions

5.2.1 Bistable Critical Thickness with Double Free Boundary Conditions

Based on the analysis of section 3, it has been found that when the dimensionless radius and dimensionless height difference of the structure are determined, as the thickness of the structure increases, the structure will change from bistable characteristics to negative stiffness (monostable) characteristics, and further to positive stiffness characteristics. Therefore there exists a bistable critical thickness and a negative stiffness critical thickness. The structure is bistable when its thickness is below the bistable critical value. Negative stiffness occurs in the structure when its thickness is less than the critical value for negative stiffness. Therefore, when the thickness of the structure is the bistable critical thickness, the minimum value of force F_{min} in the loading process is 0. That is, the dimensionless radius $\bar{r}$, the dimensionless height difference $\bar{H}$, and the dimensionless bistable critical thickness $\bar{h}_c^b$ satisfy:

$$\bar{F}_{min} = g(\bar{r}, \bar{H}, \bar{h}_c^b) = 0 \tag{19}$$

The above functional relationship can be rewritten as:

$$\bar{h}_c^b = f(\bar{r}, \bar{H}) \tag{20}$$

In order to obtain the concrete mathematical form of the above functional relationship, the script is rewritten by the following float chart (see Figure 32). The script can calculate the corresponding dimensionless bistable critical thickness value according to the determined dimensionless radius and dimensionless height difference.

Considering that when the thickness is less than the critical thickness, the structure has a bistable state and $F_{min} < 0$. When the thickness is greater than the critical thickness, the structure is non-bistable, so F_{min} is greater than 0. The above float chart adopts the 2-point method and the thickness when F_{min} is approximately equal to 0 is obtained through 10 iterations, that is, the bistable critical thickness.

Combined with the above-modified script, seven dimensionless radii (0.3, 0.4, 0.5, 0.6, 0.7, 0.8, 0.9) and seven dimensionless height differences (0.08, 0.10, 0.12, 0.14, 0.16, 0.18, 0.20), a total of 49 cases deconstructed dimensionless bistable critical thickness.

Figure 32: Float-Chart

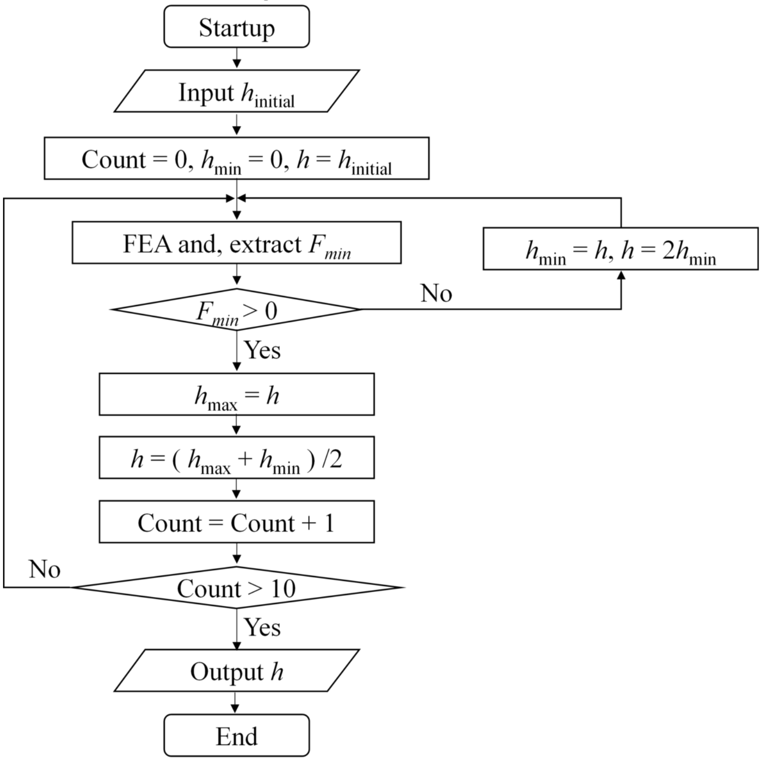

The calculation in each case is iterated 10 times, and the dimensionless bistable critical thicknesses in different cases are calculated, as shown in Figure 33.

Figure 33: The Dimensionless Bistable Stiffness Critical Thickness

$\bar{h}_c^b$		$\bar{H}$						
		0.08	0.1	0.12	0.14	0.16	0.18	0.2
$\bar{r}$	0.3	0.022	0.029	0.036	0.043	0.050	0.056	0.063
	0.4	0.024	0.031	0.038	0.045	0.052	0.059	0.066
	0.5	0.025	0.032	0.040	0.047	0.054	0.061	0.069
	0.6	0.026	0.033	0.041	0.048	0.056	0.063	0.071
	0.7	0.027	0.035	0.042	0.050	0.058	0.066	0.074
	0.8	0.028	0.036	0.044	0.053	0.062	0.071	0.080
	0.9	0.031	0.040	0.050	0.060	0.071	0.082	0.093

As shown in Figure 33, when $\bar{r} = 0.3$, $\bar{H} = 0.08$, the structures have bistability when their dimensionless thickness is less than 0.022. Colors in the graph from blue to red indicate a gradual increase in the dimensionless critical thickness. it is noticeable that as the dimensionless radius and dimensionless height difference increase, there is a gradual increase in the dimensionless critical thickness as well.

In order to obtain the critical thickness of the structure at a more general size, the specific functional relationship between them is obtained. Here, MATLAB software is used to perform function fitting on the above 49 data. Considering the applicability and accuracy of the fitting function, the following five-parameter function is used here:

$$\bar{h}_c^b = p_1^b + p_2^b\bar{r} + p_3^b\bar{H} + p_4^b\bar{r}^2 + p_5^b\bar{r}\bar{H} \tag{21}$$

The fitting results by MATLAB software are as follows: $p_1^b = 0.1299$, $p_2^b = -0.05843$, $p_3^b = 0.2394$, $p_4^b = 0.04048$, $p_5^b = 0.2621$. The fitting diagram is shown in Figure 34, and the R-square of the above fitting results is 0.9925, indicating that the above function can predict the bistable critical thickness well.

Figure 34: The Fitting Diagram Of the Bistable Critical Thickness

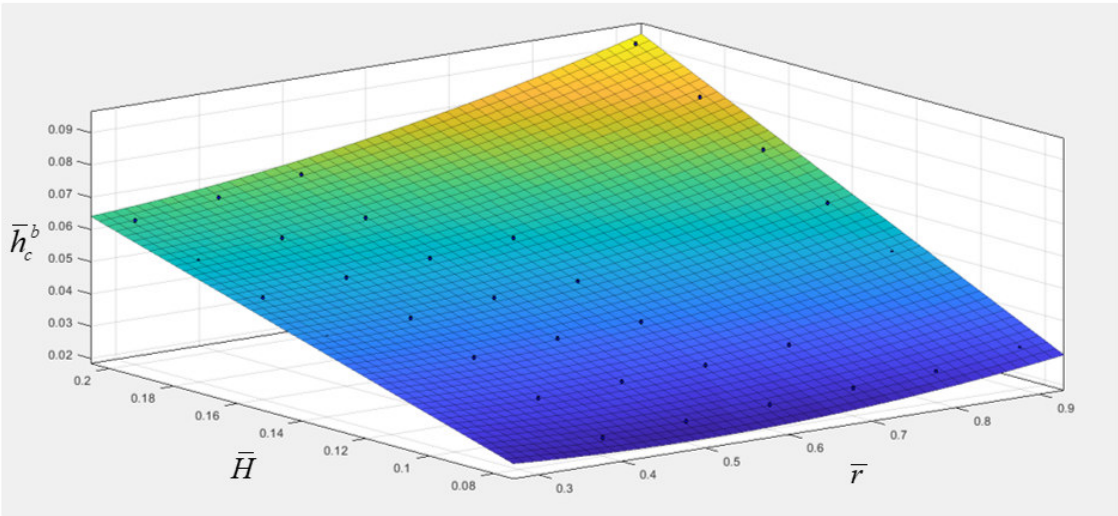

5.2.2 Negative Stiffness Critical Thickness with Double Free Boundary Conditions

To further analyze the negative stiffness critical thickness of the structure under different dimensionless radii and height differences, a method similar to the above is adopted. When the thickness is less than the critical thickness of negative stiffness, the structure has negative stiffness, and its force-displacement curve has relative maximum and relative minimum values. If the thickness is equal to or exceeds the critical thickness of negative stiffness, the structure exhibits positive stiffness, resulting in an increasing force-displacement curve without any extreme points. Therefore, the critical thickness of negative stiffness is the minimum thickness where there is no extreme point in the force-displacement curve, the judgment condition of the float chart "$\bar{F}_{min} > 0$" changed to "$\bar{F}_{min}$ does not exist".

After resubmitting the modified script, and batch calculating 7 kinds of dimensionless radii (0.3, 0.4, 0.5, 0.6, 0.7, 0.8, 0.9) and 7 kinds of dimensionless height differences (0.08, 0.10, 0.12, 0.14, 0.16, 0.18, 0.20), a total of 49 cases deconstructed dimensionless negative stiffness critical thickness. The calculation in each case is iterated 10 times, and the dimensionless negative stiffness critical thickness in different cases is calculated. As shown in the table below.

Figure 35: The Dimensionless Negative Stiffness Critical Thickness

$\bar{h}_c^b$		$\bar{H}$						
		0.08	0.1	0.12	0.14	0.16	0.18	0.2
$\bar{r}$	0.3	0.051	0.053	0.054	0.056	0.057	0.057	0.059
	0.4	0.064	0.066	0.068	0.070	0.071	0.072	0.075
	0.5	0.076	0.080	0.082	0.084	0.085	0.087	0.093
	0.6	0.089	0.093	0.096	0.098	0.100	0.103	0.111
	0.7	0.102	0.107	0.110	0.112	0.114	0.118	0.129
	0.8	0.115	0.120	0.124	0.127	0.130	0.135	0.146
	0.9	0.128	0.133	0.138	0.141	0.145	0.151	0.164

As shown in Figure 35, When $\bar{r} = 0.3$, $\bar{H} = 0.08$, the structures with dimensionless thickness less than 0.051 have negative stiffness. Colors in the graph from blue to red indicate a gradual increase in the dimensionless critical thickness. Thus, as the dimensionless radius and dimensionless height difference increase, the dimensionless critical thickness also gradually increases.

The parameters obtained by fitting the function form ($\bar{h}_c^n = p_1^n + p_2^n\bar{r} + p_3^n\bar{H} + p_4^n\bar{r}^2 + p_5^n\bar{r}\bar{H}$) of five parameters similar to the previous ones are : $p_1^n = 0.01399$, $p_2^n = -0.04473$, $p_3^n = 0.521$, $p_4^n = 0.02313$, $p_5^n = 0.3501$(R-square $= 0.9972$). Af-

Figure 36: The Fitting Diagram Of The Negative Stiffness Critical Thickness

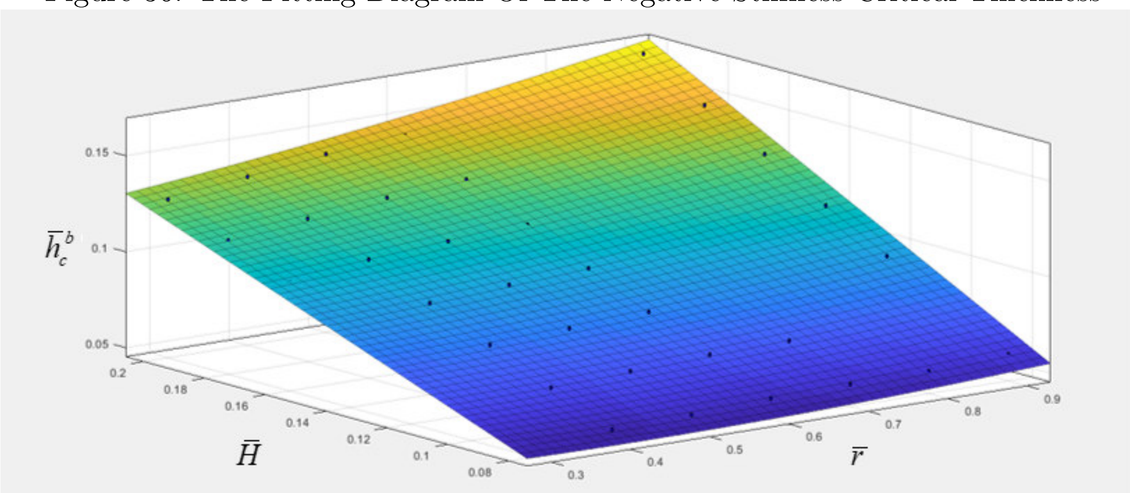

ter the above calculations, the quantitative expressions of the dimensionless bistable state and the critical thickness of negative stiffness are obtained. These expressions can quickly determine whether the truncated-conical shell has bistability or negative stiffness based on the geometric dimensions.

5.2.3 Eigenloads with Double Free Boundary Conditions

Figure 37: Force-Displacement Curve with Positive And Negative Stiffness

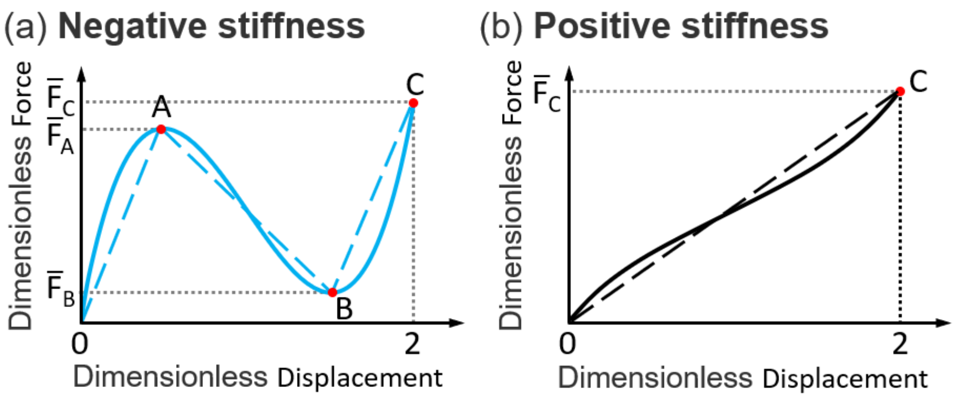

From Figure 37(a), when the structure has negative stiffness, the force-displacement curve can be approximated by the three-segment line connecting the three characteristic points A, B, and C. Among them, point A is the maximum value point, point B is the minimum value point, and point C corresponds to the loading displacement of 2 times the height difference. Define the ordinates of points A, B, and C as $\bar{F}_A$, $\bar{F}_B$, and $\bar{F}_C$, respectively. When the structure has positive stiffness, there is no extreme point in the curve, the curve can be approximated by the line connecting point C and the origin as shown in Figure 37(b).

Based on the above script, 7 dimensionless radii $(0.3, 0.4, 0.5, 0.6, 0.7, 0.8, 0.9)$ and 7 dimensionless height differences $(0.08, 0.10, 0.12, 0.14, 0.16, 0.18, 0.20)$ are calculated using the loop language, and 9 dimensionless thicknesses $(0.01, 0.02, 0.03, 0.04, 0.05, 0.06, 0.07, 0.08, 0.09)$. A total of 441 kinds of deformation processes of the structure, and a total of 386 kinds of parameter combinations under the structure with negative stiffness. In this case, the values of $\bar{F}_A$ and $\bar{F}_B$ are extracted from these 386 bistable structural force-displacement curves and the value of $\bar{F}_C$ are extracted from all the calculated data.

After analysis of the data, the relationship between $\bar{F}_A$ and $\bar{r}, \bar{H}, \bar{h}$ is difficult to be accurately described by simple functions. In order to fit the value of $\bar{F}_A$, the following function form is selected:

$$\bar{F}_A = C_1 + C_2\bar{r} + C_3\bar{H} + C_4\bar{h} + C_5\bar{r}^2 + C_6\bar{H}^2 + C_7\bar{h}^2 + C_8\bar{r}\bar{H} + C_9\bar{H}\bar{h} + C_{10}\bar{r}\bar{h} \quad (22)$$

The 10 parameters obtained by fitting MATLAB software are shown in Table 5.1(R-square = 0.9547).

C_1	C_2	C_3	C_4	C_5
0.000577	-0.001110	-0.003525	-0.006856	0.000586
C_6	C_7	C_8	C_9	C_{10}
0.006339	0.018025	0.002622	0.031584	0.005159

Table 5.1: Parameters Fitting Of $\bar{F}_A$

Similarly, choose the following function form to fit the value of F_B:

$$\bar{F}_B = C_1+C_2\bar{h}^2+C_3\bar{r}\bar{H}+C_4\bar{H}\bar{h}+C_5\bar{h}^3+C_6\bar{r}\bar{h}^2+C_7\bar{H}\bar{h}^2+C_8\bar{H}\bar{r}+c_9\bar{h}\bar{H}^2+C_{10}\bar{r}\bar{H}\bar{h} \quad (23)$$

The 10 parameters obtained by fitting are as follows(R-square = 0.9413): To

C_1	C_2	C_3	C_4	C_5
-0.000046	-0.095653	0.001642	0.047722	0.040988
C_6	C_7	C_8	C_9	C_{10}
0.122978	0.517114	-0.001181	-0.225772	-0.064393

Table 5.2: Parameters Fitting Of $\bar{F}_B$

extract the above 441 cases, F_C selects the following function form:

$$\bar{F}_C = C_1\bar{h}+C_2\bar{h}^2+C_3\bar{H}\bar{h}+C_4\bar{r}\bar{h}+C_5\bar{H}^3+C_6\bar{h}^3+C_7\bar{r}\bar{h}^2+C_8\bar{H}\bar{h}^2+c_9\bar{h}\bar{r}^2+C_{10}\bar{h}\bar{H}^2 \quad (24)$$

The 10 parameters obtained by fitting are as follows(R-square = 0.9930):

C_1	C_2	C_3	C_4	C_5
0.005788	-0.101029	-0.002177	-0.015498	0.001817
C_6	C_7	C_8	C_9	C_{10}
0.447841	0.096580	0.384841	0.010616	-0.040841

Table 5.3: Parameters Fitting Of $\bar{F}_C$

5.3 Double Simply Supported Boundary Conditions

In this section, the deformation of truncated-conical shells with double simply supported boundary conditions is studied. The pre-calculation results show that when the dimensionless radius and dimensionless height difference are large, the predetermined calculation cannot be completed, that is, the structure in this case cannot complete the predetermined deformation.

After calculation, 378 structures with different dimensionless parameters are bistable, including 6 dimensionless radii (0.3, 0.4, 0.5, 0.6, 0.7, 0.8), 7 dimensionless height differences (0.08, 0.10, 0.12, 0.14, 0.16, 0.18, 0.20), and 9 dimensionless thicknesses (0.01, 0.02, 0.03, 0.04, 0.05, 0.06, 0.07, 0.08, 0.09). Compared with the double-free boundary condition, the structure has a larger bistable critical thickness under the double simply supported boundary condition. In order to better describe the deformation characteristics of different structures with double simple supported boundary conditions, the function fitting is carried out on the relationship between $\bar{F}_A$, $\bar{F}_B$, and $\bar{F}_C$ and the geometric dimensions.

Through the observation of 378 sets of calculation results, it is found that the relationship between characteristic forces and geometric dimensions is more complicated. Considering the accuracy of the fitting function, the following 16 parameter function relationships are used to fit the value of $\bar{F}_A$:

$$\begin{aligned}\bar{F}_A =& C_1\bar{r} + C_1\bar{H} + C_1\bar{h} + C_4\bar{r}^2 + C_5\bar{H}^2 + C_6\bar{h}^2 + C_7\bar{r}\bar{H} + C_8\bar{r}\bar{h} + C_9\bar{r}^3 + \\ & C_{10}\bar{h}^3 + C_{11}\bar{r}\bar{H}^2 + C_{12}\bar{r}\bar{h}^2 + C_{13}\bar{H}\bar{h}^2 + C_{14}\bar{h}\bar{r}^2 + C_{15}\bar{h}\bar{H}^2 + C_{16}\bar{r}\bar{H}\bar{h}\end{aligned} \tag{25}$$

Using the MATLAB software 16 parameters(R-square = 0.9460) are obtained:

C_1	C_2	C_3	C_4	C_5	C_6	C_7	C_8
0.079070	-0.327142	0.564979	-0.169870	1.289386	-2.807863	0.438511	-2.172260
C_9	C_{10}	C_{11}	C_{12}	C_{13}	C_{14}	C_{15}	C_{16}
0.087087	-3.568607	-1.774718	4.889002	11.141784	1.527155	-7.533183	3.125601

Table 5.4: Parameters Fitting Of $\bar{F}_A$

Similarly, when fitting the value of $\bar{F}_B$, the following function form is selected:

$$\begin{aligned}\bar{F}_B =& C_1 + C_2\bar{r} + C_3\bar{H} + C_4\bar{h} + C_5\bar{r}^2 + C_6\bar{H}^2 + C_7\bar{h}^2 + C_8\bar{H}\bar{h} + C_9\bar{r}\bar{h} + \\ & C_{10}\bar{h}^3 + C_{11}\bar{r}\bar{H}^2 + C_{12}\bar{r}\bar{h}^2 + C_{13}\bar{H}\bar{h}^2 + C_{14}\bar{h}\bar{r}^2 + C_{15}\bar{h}\bar{H}^2 + C_{16}\bar{r}\bar{H}\bar{h}\end{aligned} \tag{26}$$

The 16 parameters obtained by fitting are as follows(R-square = 0.9361):

C_1	C_2	C_3	C_4	C_5	C_6	C_7	C_8
0.013519	-0.048759	0.023854	-0.788320	0.036403	-0.313294	3.599012	1.452916
C_9	C_{10}	C_{11}	C_{12}	C_{13}	C_{14}	C_{15}	C_{16}
2.477434	1.991095	0.370642	-5.329294	-12.564593	-1.669571	4.190060	-3.752300

Table 5.5: Parameters Fitting Of $\bar{F}_B$

The functional form of 5 parameters is used to fit the value of F_C:

$$\bar{F}_C = C_1 + C_2\bar{h} + C_3\bar{H}^2 + C_4\bar{h}^2 + C_5\bar{H}\bar{h} \tag{27}$$

The five parameters obtained by the fitting are as follows(R-square = 0.9576):

C_1	C_2	C_3	C_4	C_5
0.000057	-0.004522	-0.001428	0.059799	0.013192

Table 5.6: Parameters Fitting Of $\bar{F}_C$

5.4 Double Fixed Boundary Conditions

Similar to the previous section, this section focuses on truncated-conical shells under double-supported boundary conditions. The pre-calculation results show that when the dimensionless radius and thickness are small and large at the same time, the truncated-conical shell cannot complete the predetermined calculation process, that is, the structure at this time is difficult to undergo the predetermined deformation. The structure's deformation process under 280 cases is studied, with 5 dimensionless radii (0.3, 0.4, 0.5, 0.6, 0.7), 7 dimensionless height differences (0.08, 0.10, 0.12, 0.14, 0.16, 0.18, 0.20), and 8 dimensionless thicknesses (0.02, 0.03, 0.04, 0.05, 0.06, 0.07, 0.08, 0.09). Excluding 11 cases of calculation failure, there are 66, 229, and 40 kinds of truncated-conical shells with bistability, negative stiffness, and positive stiffness, respectively.

Observing the above 269 calculation results, it is found that when the dimensionless radius and dimensionless height difference of the structure are determined, as the dimensionless thickness increases, the structure will gradually change from bistable to negative stiffness and then to Positive stiffness.

5.4.1 Bistable Critical Thickness with Double Fixed Boundary Conditions

Similar to the previous method, five dimensionless radii (0.4, 0.5, 0.6, 0.7, 0.8) and seven dimensionless height differences (0.08, 0.10, 0.12, 0.14, 0.16, 0.18, 0.20) are calculated in batches through the loop statement, a total of 35 cases deconstructed dimensionless bistable critical thickness. The calculation in each case is iterated 10 times, and the dimensionless bistable critical thickness in different cases is calculated(see Figure 38).

Figure 38: The Dimensionless Bistable Critical Thickness

$\bar{h}_c^b$		$\bar{H}$						
		0.08	0.1	0.12	0.14	0.16	0.18	0.2
$\bar{r}$	0.4	0.020	0.026	0.031	0.036	0.041	0.046	0.050
	0.5	0.022	0.028	0.033	0.038	0.043	0.048	0.052
	0.6	0.023	0.029	0.034	0.039	0.043	0.048	0.052
	0.7	0.024	0.029	0.033	0.038	0.042	0.045	0.049
	0.8	0.023	0.027	0.031	0.034	0.037	0.040	0.043

Colors in the graph from blue to red indicate a gradual increase in the dimensionless bistability critical thickness. It is observed from the figure that as the dimensionless height difference gradually increases, the dimensionless bistable critical thickness also gradually increases. However, with the increase of the dimensionless radius, the dimensionless bistable critical thickness presents a trend of first increasing and then decreasing.

5.4.2 Negative Wtiffness Critical Thickness with Double Fixed Boundary Conditions

Similarly, five dimensionless radii (0.3, 0.4, 0.5, 0.6, 0.7) and seven dimensionless height differences (0.08, 0.10, 0.12, 0.14, 0.16, 0.18, 0.20) are calculated in batches through the loop statement, totaling 35 Deconstructed dimensionless negative stiffness critical thickness for the medium case. The dimensionless negative stiffness critical thickness calculated under different conditions is shown in Figure 39.

From Figure 39, it can be seen that as the dimensionless radius and dimensionless height difference increase, the dimensionless critical thickness also gradually increases.

Figure 39: The Dimensionless Negative Stiffness Critical Thickness

$\bar{h}_c^b$		$\bar{H}$						
		0.08	0.1	0.12	0.14	0.16	0.18	0.2
$\bar{r}$	0.3	0.053	0.066	0.079	0.093	0.105	0.119	0.132
	0.4	0.054	0.068	0.082	0.095	0.108	0.122	0.136
	0.5	0.055	0.069	0.082	0.096	0.111	0.125	0.139
	0.6	0.056	0.070	0.084	0.098	0.112	0.127	0.143
	0.7	0.056	0.070	0.085	0.100	0.117	0.141	0.171

5.4.3 Eigenloads with Double Fixed Boundary Conditions

Similar to the previous one, the expression of characteristic force is fitted based on the above 269 groups of calculation results.

The following function form is selected to fit the value of $\bar{F}_A$:

$$\bar{F}_A = C_1\bar{h} + C_2\bar{H}\bar{h} + C_3\bar{r}\bar{h} + C_4\bar{h}^3 + C_5\bar{r}\bar{h}^2 + C_6\bar{H}\bar{h}^2 + C_7\bar{h}\bar{r}^2 + C_8\bar{r}\bar{H}\bar{h} \tag{28}$$

The 8 parameters obtained by fitting are as follows(R-square = 0.9689): The function

C_1	C_2	C_3	C_4
0.247299	-0.859633	-1.070955	-10.292245
C_5	C_6	C_7	C_8
2.515078	4.385819	0.865290	2.053095

Table 5.7: Parameters Fitting Of $\bar{F}_A$

form for fitting the $\bar{F}_B$ value is as follows:

$$\bar{F}_B = C_1\bar{h} + C_2\bar{h}^2 + C_3\bar{H}\bar{h} + C_4\bar{r}\bar{h} + C_5\bar{h}^3 + C_6\bar{r}\bar{h}^2 + C_7\bar{H}\bar{h}^2 + C_8\bar{h}\bar{r}^2 + C_9\bar{h}\bar{H}^2 + C_{10}\bar{r}\bar{H}\bar{h} \tag{29}$$

The 10 parameters obtained by fitting are as follows(R-square = 0.9566): In order to

C_1	C_2	C_3	C_4	C_5
0.152132	-2.720025	0.329899	-0.546575	8.783564
C_6	C_7	C_8	C_9	C_{10}
4.972035	0.800058	0.446737	-0.567250	-0.575058

Table 5.8: Parameters Fitting Of $\bar{F}_B$

fit the value of $\bar{F}_C$, the following function form is selected:

$$\bar{F}_C = C_1\bar{h}^2 + C_2\bar{r}\bar{h} + C_3\bar{h}^3 + C_4\bar{r}\bar{h}^2 + C_5\bar{h}\bar{r}^2 + C_6\bar{r}\bar{H}\bar{h}; \tag{30}$$

The 6 parameters obtained by fitting are as follows(R-square = 0.9594):

C_1	C_2	C_3	C_4	C_5	C_6
2.133632	-0.931650	-17.979518	3.386917	1.055409	1.781479

Table 5.9: Parameters Fitting Of $\bar{F}_C$

6 Experimental Verification on Bistable Characteristics of Truncated-Conical Shells

In this section, experiments are carried out with a truncated-conical shell printed in 3D to verify the above analysis results. The experimental determination of the force-displacement curve of the truncated-conical shell during the overturning loading process needs to rely on precise and complex measuring instruments, which is difficult to achieve. Therefore, in this section, the experimental verification of whether the bistable state exists in the truncated-conical shell under different geometric sizes is carried out.

6.1 Double Free Boundary Conditions

In section 3.2, the influence of thickness on the deformation of truncated conical shells under free boundary conditions is discussed. When $R = 10mm$, $r = 8mm$, and $H = 1mm$, the structures with a thickness of $0.3mm$ or less are bistable, and the structures with a thickness of $0.4mm$ or more are monostable. Experiments can easily verify the structure's bistability. Considering the accuracy of 3D printing TPU material, it is difficult to accurately produce the truncated-conical shell with the above thickness. Four truncated-conical shell structures are produced by magnifying the above-mentioned geometric dimensions by three times. They have $R = 30mm, r = 24mm, H = 3mm$, and thicknesses of $0.6, 0.9, 1.2, 1.5mm$ respectively.

Therefore, the above-mentioned geometric dimensions are magnified by three times to produce four truncated-conical shell structures with $R = 30mm$, $r = 24mm$, $H = 3mm$, and thicknesses of 0.6, 0.9, $1.2mm$, and $1.5mm$ respectively. Based on the above analysis, only the structures with thicknesses of $0.6mm$ and $0.9mm$ have bistability.

In order to better demonstrate the deformation of the deconstruction, four lines are drawn on the inner surfaces of the four truncated-conical shell marks. Turn the inside and outside of these four structures by hand, and then place them on the table. If a structure can be stabilized in this inside-out flip, it possesses bistability.

Figure 40: 3D Printed Truncated-Conical Shells with Different Thicknesses

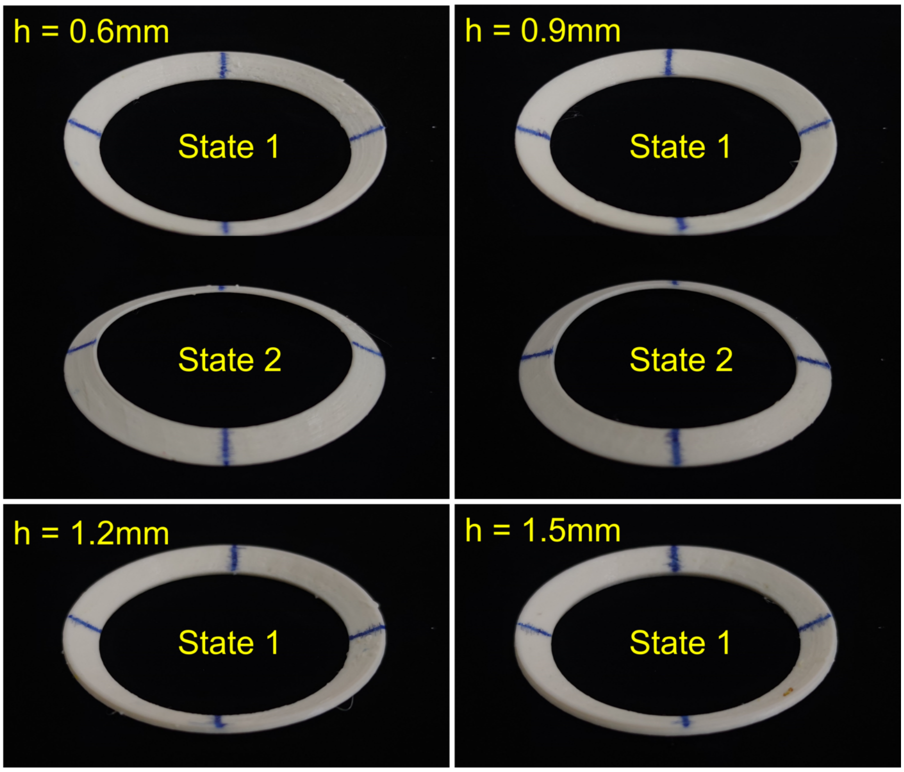

As shown in Figure 40, the experimental results show that only the structures with thicknesses of $0.6mm$ and $0.9mm$ have the second stable state inside-out. However, the structures with thicknesses of $1.2mm$ and $1.5mm$ recover quickly after releasing the external force, so they do not have bistability.

The bistable critical thickness of the truncated-conical shell under double free boundary conditions is further verified experimentally. Six structures are printed($R = 30mm$, $r = 12, 18, 24mm$, $H = 4.2, 5.4mm$). Considering the precision of the 3D printed structures, the thickness of each structure is slightly smaller than the bistable critical thickness.

The experimental results confirm the bistability of all six truncated-conical shells. Figure 41 shows the two stable states before and after the inside and outside of these eight structures are flipped.

Figure 41: Stable States of truncated-conical shells with Double Free Boundary Conditions ($R = 30mm$)

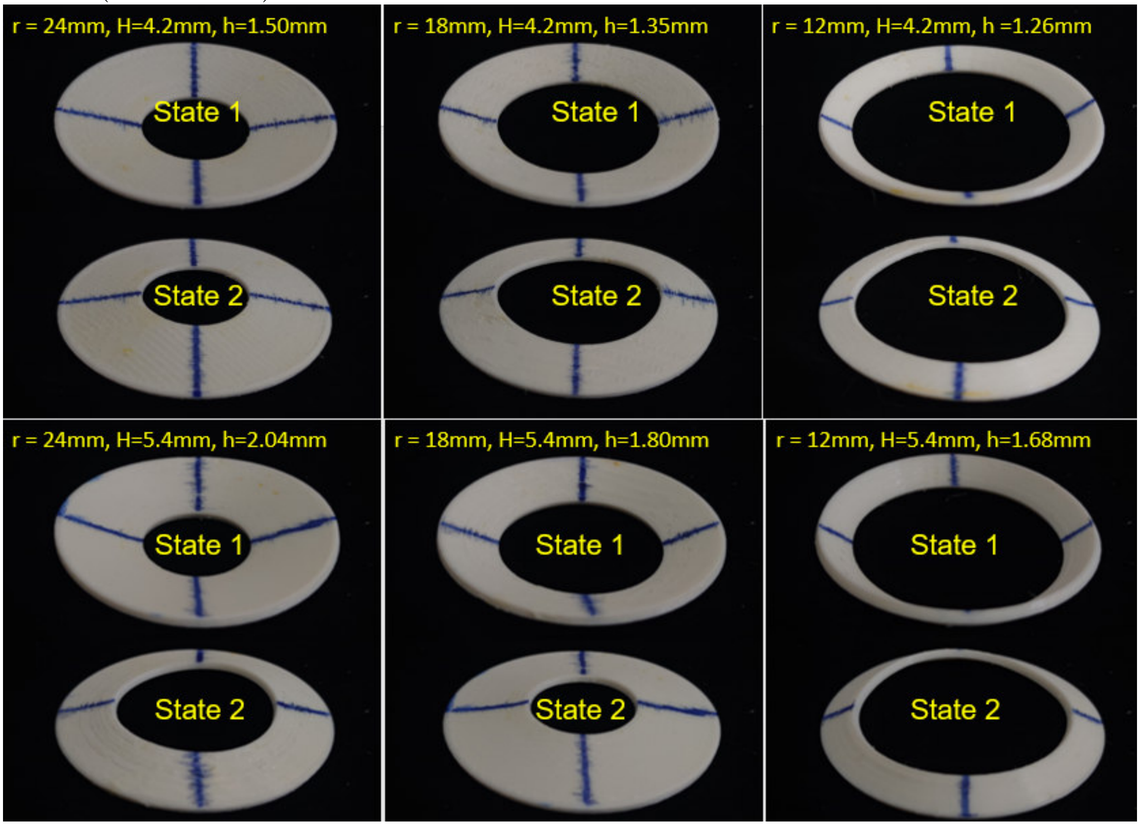

6.2 Double Simply Supported Boundary Conditions

To realize the deformation condition under the condition of the double simply supported structure, the method of dual material 3D printing is used to produce the truncated-conical shell with a constrained structure.

As shown in Figure 42, the truncated-conical shell is printed with soft TPU material (white), and the inner and outer restraint structures are printed with rigid PLA material (yellow). There is only a very small part of the connection between the two structures, that is, the constrained structure only restricts the displacement of the inner and outer circular boundaries of the truncated-conical shell but does not restrict the rotation.

The results of section 5.3 show that the bistable critical thickness of the structure is very large under the double simply supported boundary condition. Four truncated-conical shells are used($R = 30mm, r = 12, 18mm, H = 3, 4.2mm, h = 1mm$). The experimental results show that all four structures have bistability, which is consistent with the simulation results. The bistability phenomenon of these four structures is

Figure 42: Schematic Diagram of Simply Supported Boundary Conditions

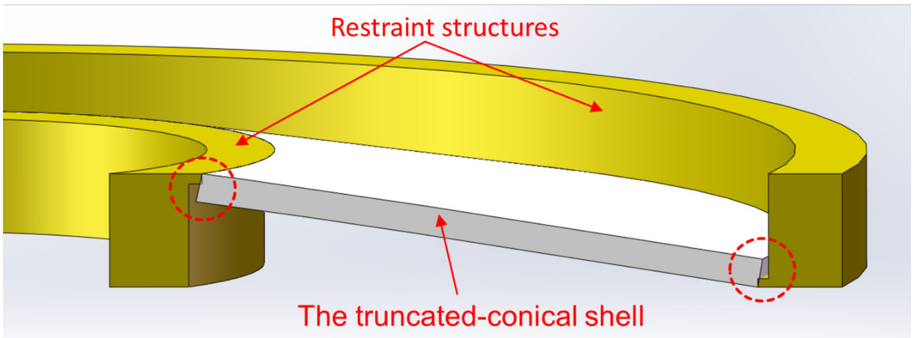

shown in Figure 43.

Figure 43: Stable States of Truncated-Conical Shells with Double Simply Supported Boundary Conditions($R = 30mm$)

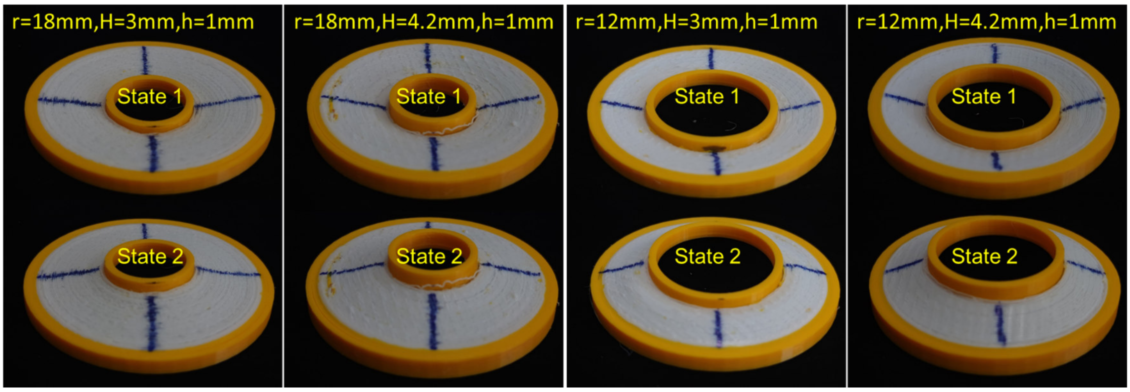

6.3 Double Fixed Boundary Conditions

Here, a dual-material 3D printing method is also used to produce a truncated-conical shell with a double-fixed support constraint structure.

The difference from the previous ones is that the inner and outer constrained structures printed by PLA material are completely connected with the truncated-conical shell printed by TPU material, that is, the constrained structure not only limits the displacement of the inner and outer circular boundaries of the truncated-conical shell, but also limits its rotation(see Figure 44). Based on the results in section 5.4, a total of 4 truncated-conical shells with $R = 30mm$, $r = 12, 18mm$, $H = 3, 4.2mm$ are made. Their thicknesses are slightly less than the bistable critical thicknesses.

The experimental results show that all four structures have bistability, which is consistent with the simulation results(see Figure 45).

Figure 44: Schematic Diagram of Double Fixed Boundary Conditions

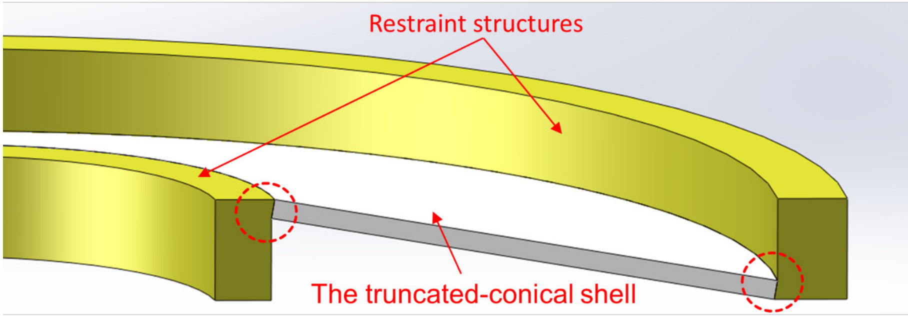

Figure 45: Stable States of Truncated-Conical Shells with Double Fixed Boundary Conditions($R = 30mm$)

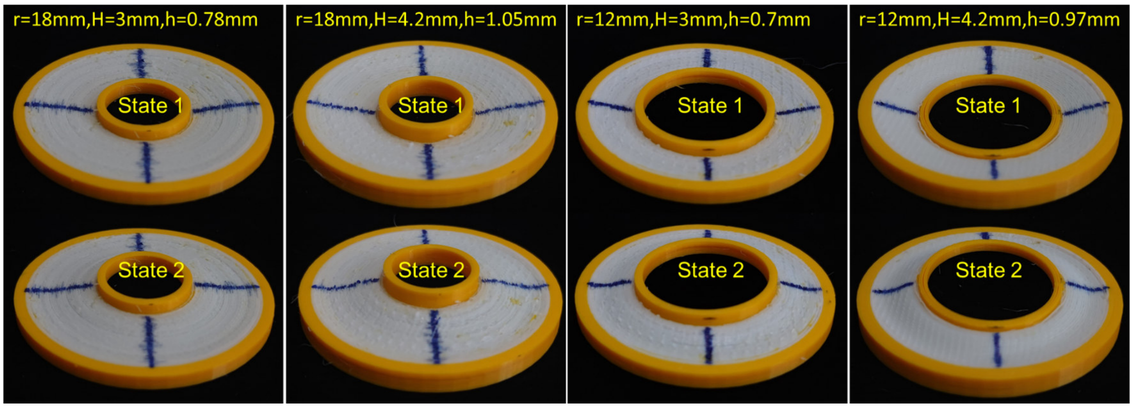

7 Conclusion

This study presents an in-depth investigation into the deformation dynamics of truncated-conical shells, specifically focusing on the underlying mechanisms resulting in a bistable state and exhibiting negative stiffness. A comprehensive quantitative model, detailing the deformation characteristics of such shells, has been formulated.

Firstly, a parametric simulation method of the truncated-conical shell is established based on Python script and FEM. Utilizing this robust methodology, we elucidated the intricate interplay of materials, geometric constraints, and boundary conditions on the deformational behavior of the truncated-conical shell. A foundational deformation theory was thus crafted, emphasizing the salient features of bistable and negative stiffness deformation. It is noteworthy that this theoretical construct primarily caters to truncated-conical shells characterized by dual-free boundary conditions.

In order to obtain a quantitative description of structural deformation characteristics, a script for batch modeling, calculation, and data processing integration was first established, and The deformations of truncated-conical shells with different boundary conditions and geometric sizes were computed. Then, based on many simulation results, the quantitative expressions of dimensionless bistability and negative stiffness critical thickness of truncated-conical shells are established based on dimensional analysis. Further, the quantitative description of the deformation characteristic force of the truncated-conical shell is established. The analysis conclusions were verified experimentally by 3D printing various truncated-conical shells.

The research results in this paper provide a reference for the design of bistable or negative stiffness structures. The expressions obtained in Section 5 can help engineers quickly judge whether the truncated-conical shell of a specific size has bistable and negative stiffness characteristics, as well as the characteristic forces. In addition, the analysis method in this paper can also be used to analyze the bistability or negative stiffness characteristics of other structures.

Acknowledgment

The straws in the drink shop can be deformed into different shapes, which aroused my interest. After discussing with my instructor Dr. Fu, we decided to study the truncated-conical shell of the straw deformation area and finally completed the project. First of all, I would like to thank my instructor, Dr. Fu for his guidance. Dr. Fu will not directly help me solve the problems when I encounter them but will encourage me to find solutions to the problems by myself, which benefits me a lot. Secondly, I also want to thank Jack Cao for his helpful suggestions and for helping me with 3D printing. Finally, I want to thank my family and friends. Their encouragement and support is also the key for me to complete this project.

References

[1] Yunteng Cao, Masoud Derakhshani, Yuhui Fang, Guoliang Huang, and Changyong Cao. Bistable structures for advanced functional systems. *Advanced Functional Materials*, 31(45):2106231, 2021.

[2] Yinding Chi, Yanbin Li, Yao Zhao, Yaoye Hong, Yichao Tang, and Jie Yin. Bistable and multistable actuators for soft robots: Structures, materials, and functionalities. *Advanced Materials*, 34(19):2110384, 2022.

[3] Douglasc. Giancoli. *Physics :: principles with applications*. Physics :: principles with applications.

[4] Yair Luxenburg and Sefi Givli. The static response of axisymmetric conical shells exhibiting bistable behavior. *Journal of Applied Mechanics*, 88(11):111001, 2021.

[5] Fei Pan, Yilun Li, Zhaoyu Li, Jialing Yang, Bin Liu, and Yuli Chen. 3d pixel mechanical metamaterials. *Advanced Materials*, 31(25):1900548, 2019.

[6] TecnoDigital School. Automate your work in abaqus using python scripts, 2023. [Online; Accessed 10 Aug. 2023.].

[7] Xiaojun Tan, Shaowei Zhu, Bing Wang, Kaili Yao, Shuai Chen, Peifei Xu, Lianchao Wang, and Yuguo Sun. Mechanical response of negative stiffness truncated-conical shell systems: experiment, numerical simulation and empirical model. *Composites Part B: Engineering*, 188:107898, 2020.

[8] Wikipedia. Buckingham theorem — Wikipedia, the free encyclopedia, 2023. [Online; Accessed 2 Aug. 2023.].